

The Small Magellanic Cloud in the far infrared^{*,**}

I. ISO's 170 μm map and revisit of the IRAS 12–100 μm data

K. Wilke, M. Stickel, M. Haas, U. Herbstmeier, U. Klaas, and D. Lemke

Max-Planck-Institut für Astronomie, Königstuhl, 69117 Heidelberg, Germany

Received 30 September 2002 / Accepted 10 December 2002

Abstract. The ISOPHOT experiment onboard the ISO satellite generated a complete view of the Small Magellanic Cloud (SMC) at 170 μm with 1.5 arcmin resolution. The map is analysed using an automated photometry program enabling accurate photometric characterization of the far infrared (FIR) emitting regions. An integrated FIR luminosity of $8.5 \times 10^7 L_{\odot}$ is obtained, leading to a star formation rate of $SFR_{\text{FIR}} = 0.015 M_{\odot}/\text{yr}$. With an average dust temperature of $\langle T_{\text{D},170/100} = 20.5 \text{ K} \rangle$, the total dust mass follows to $M_{\text{D}} = 3.7 \times 10^5 M_{\odot}$. In this paper, the sources detected at 170 μm are compared with those obtainable from the IRAS satellite data. For this purpose, the 12 μm , 25 μm , 60 μm , and 100 μm IRAS high resolution (HiRes) maps of the SMC are re-examined using the same method. In contrast to former studies, this provides an all-band ISO/IRAS source catalog which is no longer based on eyeball classification, but relies on an algorithm which is capable of automated, repeatable photometry, even for irregular sources. In the mid infrared IRAS bands numerous bright FIR emitting regions in the SMC are detected and classified: 73 sources are found at 12 μm , 135 at 25 μm (most of them with $F_{\nu} < 1.0 \text{ Jy}$). All three FIR bands at 170 μm , 100 μm , and 60 μm reproduce the overall morphological structure of the SMC similarly well, in contrast to the 12 μm and 25 μm maps which only contain a limited number of extended sources and do not trace the main body of the SMC. 243 sources are detected in the ISO 170 μm map, 155 of them with $F_{\nu} \geq 2.0 \text{ Jy}$. Comparable numbers are found for the two FIR IRAS maps at 60 μm (384) and 100 μm (338) with fluxes up to 450 Jy. 70 of the 243 170 μm sources are assigned a general SED type (“cold”, “warm”, i.e., $<30 \text{ K}$, $>30 \text{ K}$) for the first time. A comparison with earlier IRAS results suggests that many source flux densities in those studies have been under- or overestimated because of non-standardized fitting methods. Many sources with flux densities up to 40 Jy listed in former catalogs cannot be identified in our data.

Key words. galaxies: magellanic clouds – ISM: general – ISM: dust, extinction

1. Introduction

The Small Magellanic Cloud (SMC hereafter) is the smallest member of an interacting threesome of galaxies (Murai & Fujimoto 1980), the two other members of which are our Galaxy and the Large Magellanic Cloud (LMC hereafter). Due to its low mass, the SMC suffers most from the mutual disruption by gravitational forces, and as a consequence, the large scale morphology and structure exhibit distinct signs of close interactions, of which a more recent one (200 million years ago) is widely believed to be responsible for the present appearance of the SMC (Putman et al. 1998). The most prominent

morphological features are the so-called bridge (connecting the SMC and the LMC), and the Magellanic stream which extends far beyond the SMC and the LMC covering roughly 100 square degrees in the sky (Westerlund 1997).

As the nearest dwarf irregular galaxies, the SMC and the LMC serve as excellent laboratories for studying their detailed compositions since all objects in them can be assigned the same distance (50...60 kpc, see Westerlund 1997). At the same time, radio and optical data can well be obtained down to parsec and sub-parsec scales.

Both galaxies have been found to be low in dust and heavy-element abundances in comparison to the solar neighbourhood, however, high star formation rates lead to significant infrared emission from warm and cool dust. Numerous studies focus on the structural peculiarities, e.g., the extremely rich and complex HI morphology with numerous apparently expanding shells, filaments, and arcs (for results see, e.g., Martin et al. 1989, and Staveley-Smith 1997, and references therein). The SMC also hosts several giant HII regions, the referring catalog of which was produced by Davies et al. (1976).

Send offprint requests to: K. Wilke, e-mail: wilke@mpia.de

* Based on observations with ISO, an ESA project with instruments funded by ESA Member States (especially the PI countries: France, Germany, The Netherlands and the UK) and with the participation of ISAS and NASA.

** The tables in Appendices A to E are only available in electronic form at the CDS via anonymous ftp to cdsarc.u-strasbg.fr (130.79.128.5) or via <http://cdsweb.u-strasbg.fr/cgi-bin/qcat?J/A+A/401/873>

The first infrared study by Schwering & Israel 1989 (SI89 hereafter) was based on IRAS data. They found numerous new objects not listed in the IRAS published catalogs (PSC and SSS, see Beichmann et al. 1985; Helou & Walker 1985, and references therein) and compared the infrared results to catalogs obtained in different wavelength bands. The near-infrared (NIR) DENIS-based point source catalog (PSC) towards both Magellanic Clouds has recently been published by Cioni et al. (2000).

A comprehensive radio continuum study (e.g., Haynes et al. 1991; Filipovic et al. 1997, 1998a,b) addressed the question of the possible existence of magnetic fields in the SMC, the distribution of radio sources, and the comparison with other surveys (e.g., X-ray and IR data).

The LMC and SMC also became part of an ESO-SEST key programme which performed CO survey observations in both galaxies and focused on the molecular gas content and the physical properties of the molecular clouds (see, e.g., Israel et al. 1993; Rubio et al. 1993, and Lequeux et al. 1994). An X-ray source catalog can be found in Haberl et al. (2000). Comprehensive overviews of both Magellanic Clouds as well as a list of further references can be found in Westerlund (1990) and Westerlund (1997).

Since the IRAS mission the question has been raised how much (if any) cold dust exists in certain objects (e.g., star forming galaxies) which escapes a detection due to its low temperatures. The latter would cause the FIR SEDs to keep on rising significantly beyond the IRAS 100 μm band. In order to accurately determine the temperature of the cold dust in the SMC, we therefore made use of ISO's long wavelength capability and obtained a complete 170 μm map. This is the first of two papers in which the FIR properties of the SMC are discussed. In this paper, we put special emphasis on the overall SMC morphology at 170 μm , the statistical results of the ISO SMC observations, the comparison with the IRAS data, and former studies based on IRAS source catalogs. In a subsequent paper we will discuss the quantitative and detailed properties of the warm and colder dust, ranging from color temperatures and integrated FIR luminosities over dust properties of single sources to the properties of the interstellar radiation field and the star formation rates.

2. Observations and data reduction

2.1. ISO data

The observations with the ISOPHOT (Lemke et al. 1996) photometer onboard the ISO satellite (Kessler et al. 1996) were performed in January 1998 in raster mode (AOT PHT22) with the C200 detector, a 2×2 pixel array of stressed Ge:Ga with a pixel size of $89''.4$, in conjunction with the C₁₆₀ broad band filter (reference wavelength 170 μm , equivalent width 89 μm). Due to the rather large area of the SMC on the sky, the ISOPHOT observations had to be split into a mosaic of nine separate parts, each of which was accompanied by two observations of the ISOPHOT Fine Calibration Source (FCS). Adjacent parts of the whole map were designed to be slightly overlapping, while the raster step size of each part was a full detector size without any overlap.

Since there was little redundancy in the data, cosmic ray hits could mimic compact sources in the map. Therefore, instead of the standard ramp slopes from first-order polynomial fits, the pairwise differences of consecutive ramp readouts were used to derive the detector signals. This allowed a larger distribution to be analysed, leading to considerably more robust results.

To get rid of pairwise differences affected by cosmic ray hits, the robust outlier-insensitive myriad estimator (Kalluri & Arce 1998) was computed and 20% of the most deviant signals as measured by the absolute deviation were cut off. This outlier removal is similar to a median absolute deviation trimming, but instead of the initial median, the sample myriad is used to determine the outliers. The sample myriad value in turn is a robust estimator of the mode (most common value) of a distribution but does not require binning of the actual data set, and is easily computed by simply minimizing a particular cost function with a tuning constant set to a small value (for details see Kalluri & Arce 1998). After rejecting the outliers, the trimmed set of pairwise differences was linearly interpolated to a ten times finer grid and the value giving the minimum value for the myriad cost function accepted as the final signal for each raster point. This interpolation scheme was used as an approximation to a full numerical minimization of the myriad cost function.

The derived detector signals at each raster position were subsequently corrected for signal dependence on ramp integration times to be consistent with calibration observations (Laureijs et al. 2000), dark-current subtracted, and finally flux calibrated with PIA¹ Version 9.1/Cal G Version 6.0 (Gabriel et al. 1997). For the conversion to an absolute flux level, the observations of the ISOPHOT Fine Calibration Source (FCS) obtained at the beginning and end of each raster in each filter were used.

The flux calibrated data streams of the detector pixels still showed differences in the overall levels of up to 20%, mostly due to inappropriately corrected pixel-to-pixel sensitivities (flat field). If not removed, these varying brightness levels would lead to striping and chessboard-like patterns in the maps. Robust morphological filtering techniques (Sternberg 1986) were used to extract the overall level of the four data streams, which were then brought to a common mean level, thereby giving the relative pixel scaling factors.

Eventually, a complete map of the whole SMC was produced from the flatfielded flux-calibrated data streams of all pixels by using the Drizzle Mapping Method (Hook & Fruchter 2002) within IRAF², which took into account the pixel sizes and inter-pixel distances of the C200 detector and the detector roll angle. The pixel size used for the final full map was $80''$, the smallest possible size which did not produce uncovered holes. This final map was restored using the modified

¹ The ISOPHOT data presented in this paper were reduced using PIA, which is a joint development by the ESA Astrophysics Division and the ISOPHOT Consortium. The ISOPHOT Consortium is led by the Max-Planck-Institut für Astronomie, Heidelberg.

² IRAF is distributed by the National Optical Astronomy Observatories, which are operated by the Association of Universities for Research in Astronomy, Inc., under cooperative agreement with the National Science Foundation.

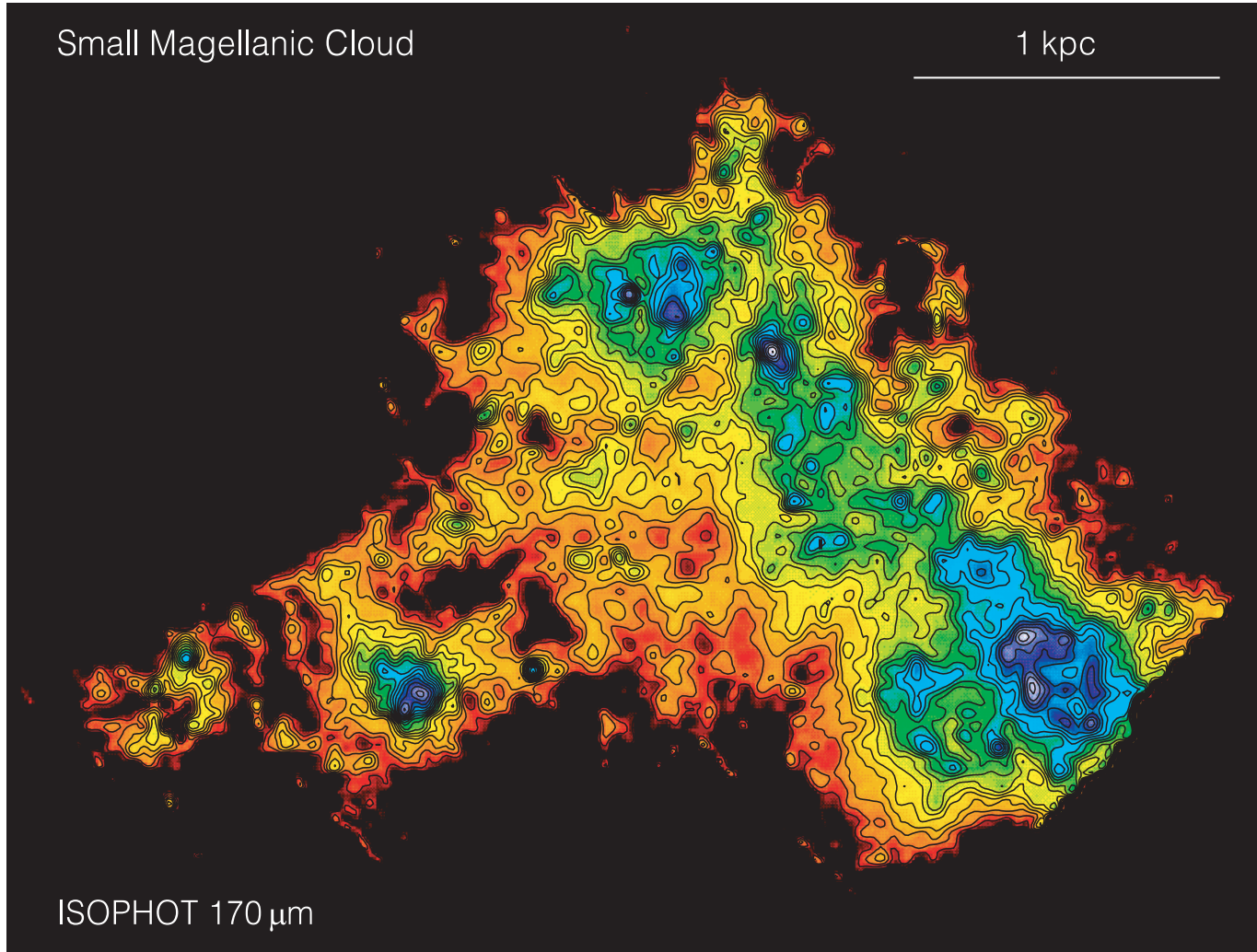


Fig. 1. False color representation of the $170\ \mu\text{m}$ ISO SMC map. Logarithmic contours are overplotted at intensities 0.04, 0.06, 0.08, 0.13, 0.20, 0.30, 0.47, 0.72, 1.11, 1.70, 2.63, 4.04, 6.22, 9.58, 14.76, 22.73, and $35.00\ \text{Jy/pix}$ (pixel size is $40''$). In order to ensure the compatibility with the IRAS HiRes data, the map was constructed from nine smaller ISOPHOT C200 maps with a resulting pixel size of $40''$ after the restoration process. Note that in contrast to the IRAS maps, the effective resolution of the restored ISO map is perfectly symmetric. The image is morphologically dominated by the main body of the SMC (the bar), to the east the so-called “bridge” (connecting the SMC with the LMC) with numerous bright and extended sources is visible. The FIR emission is dominated by several bright star forming regions in the SMC main body (dark blue/white), surrounded by regions of moderate intensity (green). The ISOPHOT observations did not cover the SW region to full extent.

Richardson-Lucy-Algorithm (Hook et al. 1994) with an additional subsampling of two pixels and a point spread function approximated by a Gaussian with a $FWHM$ of $2'$, giving a final restored map with $40''$ pixel size. This map is shown in Fig. 1.

To allow for a direct comparison with the shorter wavelength IRAS HiRes maps (see below), restored ISOPHOT (sub-)maps with the same center and size as the IRAS sub-fields were created as well as with a pixel size of $30''$. This is twice the IRAS HiRes pixel size, so that IRAS maps exactly aligned with the ISO sub-fields could be constructed by a simple 2×2 pixel block-averaging.

Although a more quantitative analysis of the FIR properties of the SMC will be performed in subsequent paper, Table 1 lists some preliminary global quantities. Remarkable are the numbers found for the global star formation rate, and the

gas-to-dust ratio resulting from the additional cold dust component entering the total dust mass.

2.2. IRAS data

While $12\ \mu\text{m}$ and $25\ \mu\text{m}$ images trace mainly hot HII regions and foreground stars with little diffuse IR emission, FIR maps ($60\ \mu\text{m}$ and $100\ \mu\text{m}$ IRAS observations) show a lot of diffuse emission with a wealth of filamentary structure.

Although source catalogs for this wavelength range were published in the past already (for an extensive comparison of IRAS SMC source catalogs with other wavelength bands see, e.g., S189), we decided to re-analyse the IRAS high resolution (HiRes hereafter) data in order to treat ISO results and IRAS data in an identical and reproducible way. Since the area in the

Table 1. Global properties of the SMC, derived from the 170 μm ISO and the 100 μm IRAS map. Both data sets were used to construct a color temperature map the referring average dust temperature $\langle T_{\text{D},170/100} \rangle$ was derived from. Dust masses were computed using a $\kappa(\beta, 170 \mu\text{m}) = 21.6 \text{ cm}^2 \text{ g}^{-1}$, according to the method presented in Klaas et al. (2001). An average grain size of $a = 0.1 \mu\text{m}$ was used, the grain density was assumed to be 3 g cm^{-3} . Note that we used $\beta = 2$ for our computations. A lower emissivity index would lead to larger values for κ , hence to dust masses M_{D} which are smaller than for $\beta = 2$.

F_{40-220}	$5.6 \times 10^{-10} \text{ W/m}^2$
F_{1-1000}	$7.6 \times 10^{-10} \text{ W/m}^2$
L_{1-1000}	$8.5 \times 10^7 L_{\odot}$
SFR	$0.0148 M_{\odot}/\text{yr}$
$\langle T_{\text{D},170/100} \rangle$	20.5 K
M_{D}	$3.7 \times 10^5 M_{\odot}$
$M_{\text{gas}}/M_{\text{dust}}$	≈ 1140

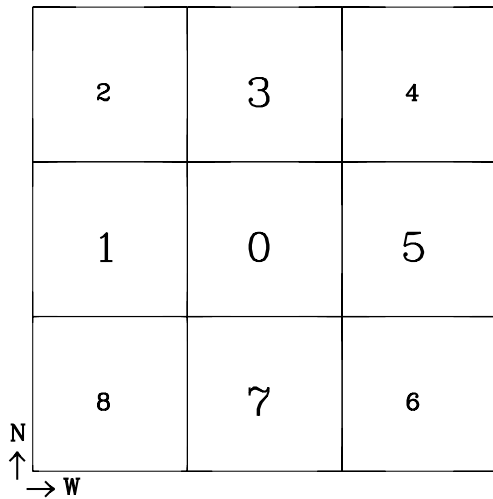


Fig. 2. Orientation of the $2^\circ \times 2^\circ$ degree IRAS HiRes fields in the sky. Centering the SMC on field 0 meant that it covered most of the central body, though not the total area of the SMC. In order to make our source catalogs as complete as possible, all fields containing SMC objects (0, 1, 3, 5, 7) were therefore used for further analysis. Fields 2, 4, 6, and 8 turned out to be devoid of any objects and have therefore not been considered.

sky covered by the SMC is comparably large ($6^\circ \times 8^\circ$ in the optical) and IRAS HiRes data can be requested with maximum field sizes of $2^\circ \times 2^\circ$ only, we split up the SMC field into 9 single $2^\circ \times 2^\circ$ fields with the central one covering most of the central body of the SMC in the FIR (for the orientation of the fields in the sky see Fig. 2). This ensured that the borderlines between two adjacent fields (though covered by a small overlap) would not be located in the brightest parts of the SMC. The central coordinates for the requested $2^\circ \times 2^\circ$ fields (equinox B1950.0) are given in Table 2. Pixel sizes were $15''$ for all fields.

The data reduction for the IRAS scans at IPAC comprises several steps: first, the calibrated, reconstructed detector data is deglitched (which removes spurious non-source-like signals originating from radiation impacts on the detector) and destriped (which corrects for different detector responsivities during different scans, i.e., additive offsets of certain strips). The

Table 2. Requested fields for IRAS HiRes processing. Numbers are the same as in Fig. 2, where the orientation of the fields on the sky is given. All four bands (12 μm , 25 μm , 60 μm , 100 μm) were retrieved for each field and checked for the presence of possible MIR/FIR SMC sources.

Field	RA	DEC
0	13.320000	-72.937271
1	20.093601	-72.937271
2	20.093601	-70.949771
3	13.320000	-70.949771
4	6.5463982	-70.949771
5	6.5463982	-72.937271
6	6.5493982	-74.924771
7	13.320000	-74.924771
8	20.093601	-74.924771

zodiacal emission model was then subtracted from all data scans individually. For the HiRes data fields a maximum correlation method (MCM) for the reconstruction of the original image is applied to the single scans which not only iteratively builds a reliable model of the sky brightness, but also enhances the resolution to $15''$ pixel size. For a more detailed description of IRAS data reduction routines see Assendorp et al. (1995), Bontekoe et al. (1994), and Aumann et al. (1990). All resulting IRAS maps are calibrated in MJy/sr, two of them (central 60 μm and 100 μm) are shown in Fig. 3.

The visual inspection of all nine fields yielded the result that only in five of them objects belonging to the SMC are located. These fields are oriented in a cross-like pattern in the sky with numbers 0, 1, 3, 5, and 7 (see Fig. 2). All other fields were neglected for the subsequent analysis.

3. Source detection

For the source detection and analysis, the HIIPhot package, a robust and fully automated method developed by D. Thilker was used (Thilker et al. 2000). It was originally designed for determination of positions, fluxes and sizes of HII regions on continuum-subtracted H_{α} images in galaxies. To our opinion, this program surpasses other existing algorithms in detecting overlapping sources, especially in crowded regions (e.g., DAOPHOT, Stetson 1987, or ALLFRAME, Stetson 1994 which have been tested for comparison as well). Applied to IRAS and ISO data, we benefit from several aspects of this code:

- the source detection is efficient and reproducible;
- no assumptions on the intrinsic source structure are required;
- the program provides adaptivity to the actual source morphology by making use of an iterative approach for growing sources from an initial guess at the shape and orientation;
- overlapping sources are accurately detected even in crowded fields and in the presence of a substantially inhomogeneous background (which is most important for the two MIR IRAS bands at 12 μm and 25 μm);
- the program offers the possibility of interactively selecting appropriate object and sky regions, a feature that helps to

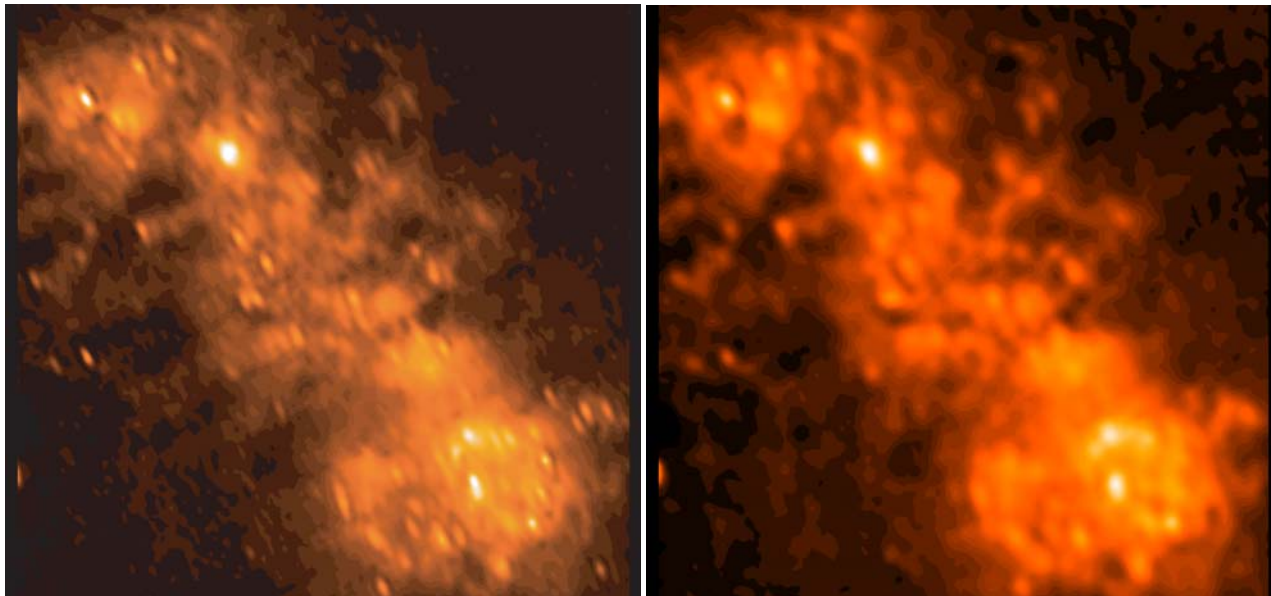


Fig. 3. IRAS HiRes maps of the SMC. Left: $60\ \mu\text{m}$ map, right: $100\ \mu\text{m}$. Since requests for IRAS HiRes maps are limited to $2^\circ \times 2^\circ$ for an individual field, the whole area of interest was split up into 9 single fields. This figure shows the central field only, but the surrounding eight other fields (see Fig. 2) were studied as well. As expected, the $100\ \mu\text{m}$ image shows a lower resolution than the $60\ \mu\text{m}$ data due to the PSF *FWHM* increase. Consequently, more isolated small-scale structure is seen in the left image.

avoid a contamination of those fields considered for background estimation by possible source candidates.

The algorithm requires a number of parameters to be set initially which are then optimized by running the code several times for all data sets in the five IR bands (four IRAS bands and one ISO band). Most important are the final *S/N* value below which a detection is not accepted, and the final gradient in surface brightness in the vicinity of the source where the growth procedure stops. All relevant parameters for the different data sets are given below.

Initially, the program defines a rank list of possible detections, to which one out of six basic morphologies, ranging from Gaussian profiles to rings with different major-to-minor axis ratios, is assigned (for an extensive discussion on the construction of the source candidate list see Thilker et al. 2000). In a next step, so-called “footprint” areas are constructed by “allowing” the program to allocate pixel areas of the SMC input image according to the morphology assigned to the source (Fig. 4a) which may contain pixels which are not bright enough to remain in the final boundary of the source after the end of the growth procedure. For this reason, “seed” regions are constructed by rejecting pixels falling below a certain median surface brightness limit of the initial “footprint” region (Fig. 4b). In a third step, iterative growth starts: pixels are considered down to a limit equal to the outermost isophote, this limit is reduced by 0.02 dex in every iteration until a certain lower limit is reached (Fig. 4c). The program offers the option of making arbitrary selections for this limit where the surface brightness profile has become “sufficiently” flat (see Fig. 4d).

The resolution of the IRAS HiRes maps is highly asymmetric, especially for the MIR range at 12 and 25 micron. Basically, this is the result of the rectangular detector mask shapes and the geometry of the scans covering the sky.

Consequently, point sources appear elongated with the narrow dimension in the scan direction and the larger dimension determined by the cross-scan-size of the detector. Since we use IRAS HiRes data, it is very difficult to determine an effective resolution, however, the resolution of *unenhanced* coadded IRAS images of approximately $1' \times 5'$, $1' \times 5'$, $2' \times 5'$, and $4' \times 5'$ for the $12\ \mu\text{m}$, $25\ \mu\text{m}$, $60\ \mu\text{m}$, and $100\ \mu\text{m}$ data provides us with an impression of which resolution changes may occur in our maps when proceeding towards longer wavelengths.

After the source catalogs were generated for every wavelength and the classification of the detected sources (the classification scheme is explained in detail in the next section), they were correlated with each other, i.e., we tried to identify sources in different catalogs within a certain correlation radius. We decided to choose a value of $r_{\text{corr}} = 90''$ due to the high spatial resolution of the ISO and IRAS data, though the average values for that radius were slightly larger in former studies (e.g., see Filipović et al. 1998b who used $r_{\text{corr}} = 2.5'$ for the comparison between IRAS and radio data). This ensured the detection of all relevant source pairs in different wavelength bands and avoided a too large number of multiple correlations at the same time, a condition which constitutes the corresponding upper limit for r_{corr} . As is clearly visible from the resulting tables which are presented in Appendices A–E, we never encountered more than 5 cross-identifications with more than one source in one band.

4. Source classification

Before we go in detail through the maps of each IR band (Sects. 5 to 9), we consider the source classification by colour temperature and other quantities, enabling us to list also the source class for most objects in the catalogs.

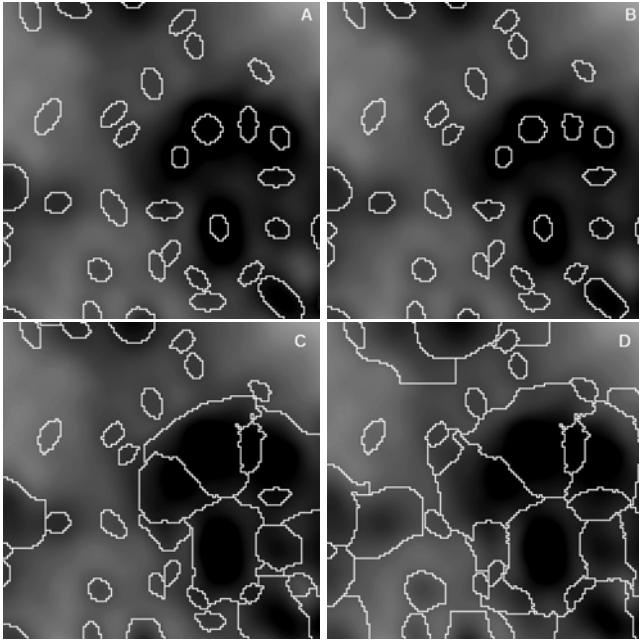


Fig. 4. Illustration of the various stages of the HIIphot procedure for a special area. **a)** IRAS 100 μm image of the SMC with “footprint” boundaries marked in white. Darker colors indicate higher flux densities. **b)** “Seed” boundaries marked. **c)** The extents of the emitting regions are shown after growth to a certain terminal surface brightness. **d)** Same as in **c)**, but for a state of growth to a terminal surface brightness well below the one used in **c)**. Note that in this last state (to a smaller extent also already in plot **c)**) the boundaries do not only contain HII regions but also the associated colder dust.

Our classification scheme relies on the ISO 170 μm data as a primary indicator and is then extended to the other four IRAS catalogs as far as possible. The full cross-correlated tables are given in Appendices A–E, for illustration purposes, an excerpt of the ISO 170 μm catalog is presented in Table 4. Only 170 μm sources with flux densities $F_\nu > 2.0$ Jy are further analysed and classified, which applies to 155 sources (in contrast to 243 sources in total). Our classification symbols always appear as the first letter in the “identifications” column.

The general classification scheme is the following: a source is labelled “C” (cold) when the color temperatures (assuming a modified black body with an emissivity of $\beta = 2$) derived from both, the 170 $\mu\text{m}/100 \mu\text{m}$ and the 100 $\mu\text{m}/60 \mu\text{m}$ ratios, are $T_{\text{BB}} < 30$ K, it is classified “W” (warm) when $T_{\text{BB}} > 30$ K is obtained in both cases. “(C)” denotes sources where a classification as “C” remains uncertain due to missing 60 μm and/or 100 μm data points. A source is labelled “Q” (questionable) when the precise shape of the SED cannot be derived due to source confusion. There are a few cases where the SED seems to “drop” between 60 μm and 170 μm due to a lower 100 μm flux density value. This behaviour has to be attributed to different PSF sizes in the different wavelength bands, leading to correlations of physically *independent* sources in the three wavelength bands.

The first letter of the identification label is followed by a down- or uparrow (\Downarrow or \Uparrow) in those cases where F_{170}/F_{100} -ratios < 1 and > 1 , respectively. Identical 170 μm and 100 μm

flux densities are indicated by a =. Note that for a “cold” BB-spectrum, i.e., $T_{\text{BB}} < 30$ K, the F_{170}/F_{100} -ratio needs not necessarily exceed 1.0.

A cross-identification with the source catalogs given by SI89 leads to the next classification letter, which may be “(C)” or “(W)”, hinting at their cold and warm sources. Note that this type of coding could in principle lead to an ambiguity in the meaning of the single-letter label “(C)”: this could either mean that a SI89 identification is referred to without any identification in our catalog or be the label for a probably cold source which is only found in our source study. In fact, all sources classified as “(C)” are assigned this source type in our catalog only, so this ambiguity is avoided.

Similar classification schemes apply to the four IRAS catalogs. In the 100 μm case, all available identifications were copied from the 170 μm catalog first. Other sources not found in the 170 μm list were then classified according to their 100 $\mu\text{m}/60 \mu\text{m}$ ratio, but down to a flux limit of 1.0 Jy only (which applies to the 60 μm catalog as well). “ \Uparrow ”, “ \Downarrow ”, and “ \odot ” indicate 100 $\mu\text{m}/60 \mu\text{m}$ flux ratios > 1 , < 1 , and ≈ 1 , respectively. For all following catalogs, identifications found for catalog entries at larger wavelengths were copied if and only if the referring source was directly identified in that catalog. When a source detected at 60 μm is identified with a source at 100 μm , the 170 μm counterpart identifications of the 100 μm source will be accepted for the 60 μm catalog only if the 60 μm source is *directly correlated* and therefore listed in the 170 μm catalog as well.

Our sources detected by HIIphot in all five bands were cross-correlated with the SIMBAD database in order to identify well-known HII regions, X-ray sources, etc. The SIMBAD database was searched using a correlation radius of 60” for all catalogs (which is different from the *coordinate* correlation radius of 90” used in our IR study). From a large list of possible identifications the most important catalogs were included:

- IRAS sources from the point source catalog (PSC) or the Faint Source Catalog (FSC) are referred to by the label IRAS and the corresponding catalog entry number (e.g., IRAS 00403-7316);
- HII region identifications are taken from the sample of Davies et al. (1976) and labelled HII DEM with the identification number from that catalog, e.g., HII DEM SS161n;
- Cross-identifications with several catalogs of emission-line stars are marked Em*. The following catalogs may occur: LIN or MA93 for a source from the catalog of emission-line stars and small nebulae in the SMC by Meyssonnier & Azzopardi (1993), AM77 for a catalog entry from the catalog of supergiant stars by Ardeberg & Maurice (1977), LHA for the catalog of H α emission stars and nebulae in the MCs by Henize (1956), AzV for entries from the catalog of SMC star members by Azzopardi & Vigneau (1982);
- If one of the above catalogs classifies the source not as emission-line star, but as emission object, it is labelled EmO with the same catalog acronyms;
- X-ray identifications are labelled “X” with the referring catalog identifiers in brackets: ROSAT sources are labelled “RX”, e.g., RX J0059.3-7223, other labels may be used for

Table 3. This table is an excerpt from the final ISO 170 μm catalog as it is presented in Appendix E. The 170 μm source list (the master catalog, entry numbers n_5) was correlated with the four IRAS catalogs according to the source center coordinates (epoch 2000) in the 170 μm ISO catalog given in columns α and δ . If the distance between an IRAS source from any of the four catalogs and a source from the ISO list was found to be less than $90''$, the two were considered identical. F_5 and ΔF_5 denote the 170 μm flux and the 1σ error derived from the HIIphot algorithm. n_4 , n_3 , n_2 , and n_1 indicate the corresponding entry numbers in the 100 μm , 60 μm , 25 μm , and the 12 μm catalog, respectively. More than one number in these columns indicates the presence of two or more sources within the correlation radius of $90''$. For the meaning of the letters and acronyms in the last column (“identifications”) see text.

<i>ISO 170 μm source catalog</i>									
n_5	α [h m s]	δ [° ' "]	F_5	ΔF_5	n_4	n_3	n_2	n_1	identifications
1	00 41 40	-73 02 16	2.2	0.4	40 42	20 24	9		C IRAS 00395-7317
2	00 42 06	-73 08 34	0.3	0.0					
3	00 42 06	-72 59 58	4.1	0.4	50	32	14		C↑(C) IRAS 00403-7316 HII DEM S6
4	00 42 58	-72 59 36	5.5	0.5	58	39	17		Q(C) IRAS 00413-7316
5	00 43 25	-73 02 31	3.2	0.4	59	41	19		Q(W)
6	00 44 37	-72 58 06	0.7	0.3	71		20		
7	00 45 18	-73 05 23	59.8	1.6	76	56	24	15	C↑IRAS 00436-7321 Em*(AzV7)
8	00 45 21	-73 16 16	228.8	2.7	74	54	22	16	C↑ HII DEM S14 Em*(LIN72/MA93 96)
9	00 45 28	-73 22 07	259.5	0.0	75	55	23	17	C↑(C) IRAS 00435-7339 EmO(LHA 115-N 13/A/B)
10	00 46 32	-73 05 59	105.8	1.8	82	64	29	20	C↓(C) IRAS 00447-7332 HII DEM S23 Em*(AM77 9)
11	00 46 34	-73 21 23	158.0	2.4	79		28	18	C↑(C) HII DEM S24
12	00 46 35	-73 15 28	84.6	1.7	81	65			C↑ Em*(LIN79)
13	00 46 45	-73 30 51	46.1	0.0	84	68	30		C↓(C) IRAS 00449-7347
14	00 46 46	-73 09 37	93.9	1.7	83				(C)↑ Em*(LIN84/MA93 143)
15	00 47 37	-73 05 26	329.3	3.3	89				C↑
16	00 47 52	-73 15 16	453.4	3.6	91	79	34	23	C↑(C) IRAS 00462-7331 EmO(LHA 115-N 20)
17	00 47 55	-73 35 21	1.7	0.0	90	81			
18	00 47 56	-73 23 47	13.1	0.9		75 84			(C)(W) IRAS 00462-7339
19	00 47 58	-72 23 13	4.3	0.4	92	83			C↑
20	00 48 13	-73 08 01	186.2	2.4		77	32		C(C) X(HFP2/409)
21	00 48 34	-72 57 51	6.6	0.8	98	89	38		Q(W) IRAS 00467-7314
22	00 48 37	-72 26 54	0.8	0.3	97	88			
23	00 48 39	-73 19 52	32.6	1.3	96				C↑
24	00 48 52	-72 48 38	65.2	1.8	99	93			C↑
25	00 48 52	-73 08 33	269.4	3.0	100	94		26	C↑(C) Em*(MA93 265/276)
26	00 48 55	-72 54 54	12.0	1.0	101	96	40		Q Em*(MA93 262)
27	00 49 23	-73 34 27	2.6	0.5	103	97			C↑(W)
28	00 49 27	-73 26 49	34.3	1.2	110	101	43		C↑(C) IRAS 00483-7250 Em*(LHA 115-N 33)EmO(MA93 301)
29	00 49 42	-73 23 45	9.3	0.8			46		(C) X(HFP2/468) Em*(LIN 139)
30	00 49 58	-73 12 00	26.5	1.2		106			(C) X(SHP2/SMC30) Em*(MA93 335)
...
...

entries from the ROSAT HRI catalogue of X-ray sources in the SMC region by Sasaki et al. (2000, hereafter SHP), the PSPC catalogue of X-ray sources in the SMC region by Haberl et al. (2000, HFP), papers by Gotthelf et al. (1996, GHH), Inoue et al. (1983, IKT), Yokogawa et al. (2000, YIT), and Bruhweiler et al. (1987, BKGs).

In the following sections, we will discuss the general morphological aspects of the four IRAS and the ISO map, the spatial source distribution, and the corresponding source catalogs generated by HIIphot. The cross-correlation of the five catalogs and the comparison to older existing IRAS studies of the SMC are addressed in two further sections.

The question of the underlying physics in the SMC interstellar medium and the nature of single sources will be

extensively discussed in Paper II where we will also put our SMC results in the context of already existing complementary observations and catalogs, e.g., the FUV spectroscopic explorer survey of interstellar molecular hydrogen in the SMC by Tumlinson et al. (2002), HI data as analysed in Stanimirovic et al. (2000), or CO data (see, e.g., the results from the ESO-SEST key programme in the SMC given in Israel et al. 1993 and subsequent papers).

5. The 12 μm IRAS map

5.1. General remarks

As was stated in SI89 already, a reliable source detection is most difficult in the case of the 12 μm IRAS data due to the

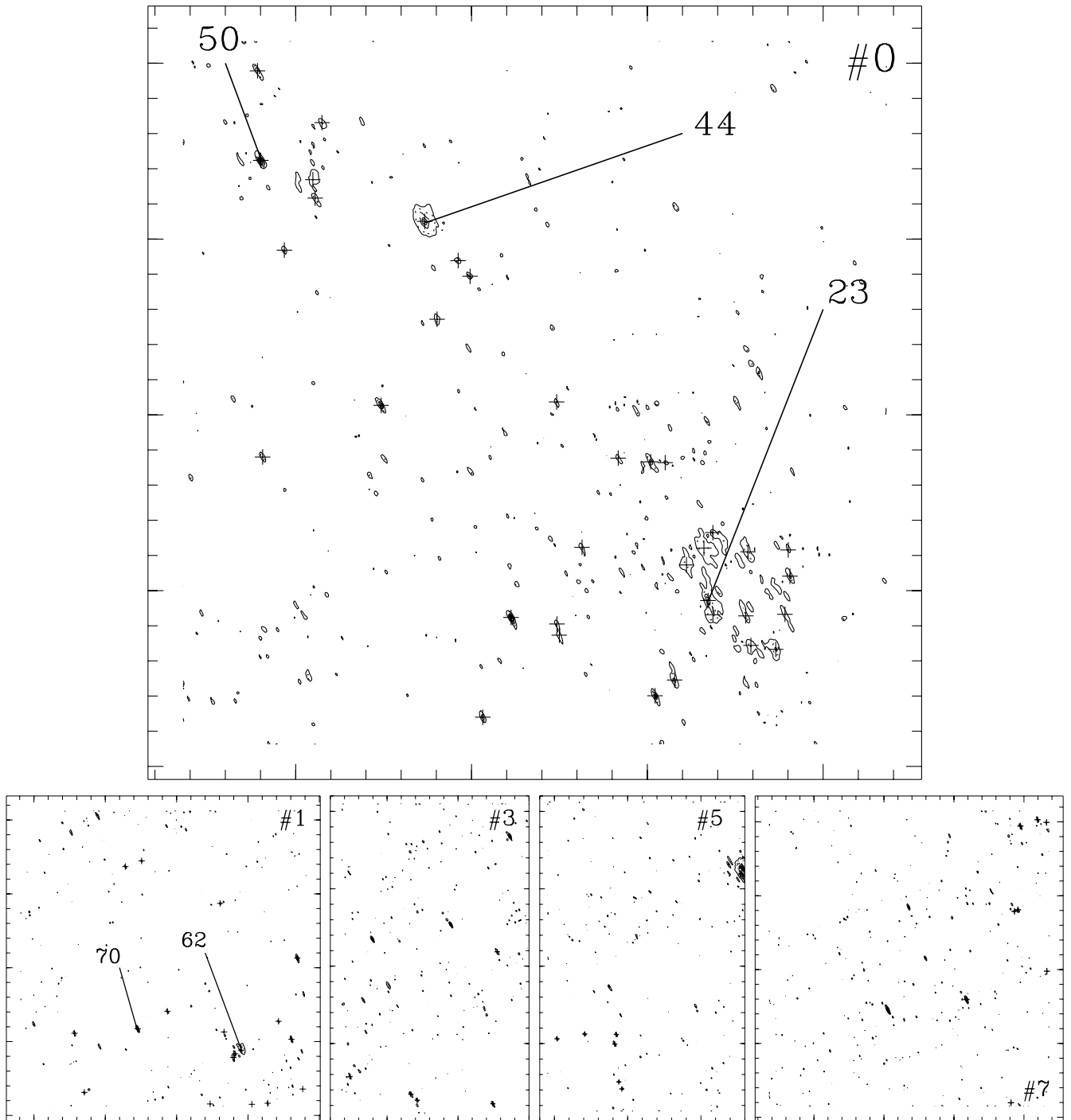


Fig. 5. $12\ \mu\text{m}$ IRAS HiRes data of the five examined SMC fields. Contours are plotted at the following flux levels: 2, 8, 16, 20, 28 MJy/sr (solid lines), 3, 10, 20, 35 MJy/sr (dotted lines), and 5, 12, 24, 40 MJy/sr (dashed lines). Upper contour plot: the central SMC field. Lower plots, from left to right: adjacent SMC fields with numbers 1, 3, 5, and 7 in eastern, northern, western, and southern direction. Sources detected by the HIIPhot algorithm are marked with a cross (+). Labelling numbers refer to the catalog entries in Appendix A.

noisy and irregular background structure. For our HIIPhot analysis, we therefore chose $S/N \geq 6.0$. The PSF $FWHM$ was assumed to be 4.0 pixels at a pixel scale of $15''/4.36\ \text{pc}$ (at a distance of 60 kpc). The maximum extension of the sources was limited to 50 pc. The projected distance for the background estimation was limited to 25 pc.

The cutoff in surface brightness was adjusted to 1.4 MJy/sr which caused the program to limit the source growth to the

visually determined size. The MIR emission in Fig. 5 (upper plot) is dominated by the presence of numerous discrete sources while nearly no diffuse emission is detected. The discrete sources are mainly located in two different regions: most of them cluster in a ring-like structure in the SW part of the SMC, and some of them are located in the NE part of the SMC bar. Most detections are found in the central IRAS field 0 (upper plot in Fig. 5). To summarize, at $12\ \mu\text{m}$ the SMC appears

as a patchy pattern of single discrete sources which are not a tracer of the morphology of this galaxy.

5.2. Source catalog and classification

73 sources were found and assigned flux densities up to ≈ 7 Jy by the HIIphot program with the vast majority of the 12 μm sources exhibiting flux densities below 1 Jy (as seen in Appendix A). The five sources labelled 23, 44, 50, 62, and 70 in Fig. 5 were assigned a growth luminosity of 1.1 Jy, 1.1 Jy, 1.5 Jy, 0.9 Jy, and 1.7 Jy, respectively. These sources were selected for labelling this and the following IRAS and ISO figures since they could be identified by the HIIphot program in all five SMC maps, thereby serving as “landmarks”. Noticeably, the two brightest 12 μm sources with luminosities of 7.1 Jy and 2.7 Jy (#25 and #57), respectively, are identified in the 25 μm data only.

As given in Table 4, 25 of our 73 sources listed in Appendix A were identified as IRAS PSC or FSC sources using the SIMBAD database within a correlation radius of 60”, 14 were classified as HII regions already in former studies. Finally, 38 sources fit into the category “emission line star/emission object”. The SIMBAD results for the identification of carbon stars are omitted in Appendix A and in Table 4, since nearly all of our sources (65) were associated to such a star within the correlation radius. 18 sources could be classified as type “C” (cold) according to the classification criteria for the 170 μm catalog given above. 14 of the sources show a 170 μm /100 μm flux ratio greater than 1.0. Of the sources which were *not* found in the 170 μm ISO map but could be classified using the 60 μm and 100 μm data, 2 have flux ratios $f_{100\mu\text{m}}/f_{60\mu\text{m}} \geq 1.0$, other two ones yield $f_{100\mu\text{m}}/f_{60\mu\text{m}} < 1.0$.

6. The 25 μm IRAS map

6.1. General remarks

For the 25 μm data, identical parameter settings as in the 12 μm case were used, with the exception of the final S/N value for the source detection (≥ 5.5). Especially the final surface brightness cutoff (1.4 MJy/sr) and the maximum size of the sources (50 pc) remained unchanged. At this longer wavelength, more sources emanate from the background, especially in the SW part of the SMC (Fig. 6). The ring-like structure, already recognizable at 12 μm , shows up as a plateau on a comparably high flux level. However, the underlying shape of the SMC still remains invisible in the central field (upper plot in Fig. 6), since there are no sources along the main body and in the outer edges of the SMC. In contrast to the 12 μm case, extended sources start to show up in the so-called “bridge” region in the eastern part of the SMC (lower row in Fig. 6, left plot).

6.2. Source catalog and classification

In total, 135 sources are detected (Appendix B) of which 60 are classified as IRAS PSC or FSC sources. 31 sources are identified as HII regions according to SIMBAD, 79 of the detections fall into the “emission line star/emission object” category.

Using the 170 μm data which is essential for determining low temperatures below ≈ 30 K, 41 have FIR SEDs which are fitted best using a blackbody with temperatures ≤ 30 K (“C”), 24 of which have $f_{170\mu\text{m}}/f_{100\mu\text{m}} \geq 1.0$, 12 fall within the range $f_{170\mu\text{m}}/f_{100\mu\text{m}} < 1.0$. Six are associated with warm (“W”) sources. 9 sources remain unclassified due to source confusion among the three FIR bands. 16 sources which are not detected in the 170 μm band have $f_{100}/f_{60} \geq 1.0$, 4 have $f_{100}/f_{60} < 1.0$. From this and Table 4 it is clearly visible that, compared to the 12 μm case, the number of cold sources as well as the number of sources with $f_{170\mu\text{m}}/f_{100\mu\text{m}} \geq 1.0$ have considerably increased.

The source counts resemble numbers and flux distribution of the 12 μm map: as can be seen from Fig. 13, the bulk of the flux densities lies in the interval 0.05 Jy . . . 1.0 Jy, although there is now a larger percentage of sources with even higher fluxes (17% of the 135 sources). Our five marked sources – again among the brightest ones – in Fig. 6 with numbers 34, 80, 87, 114, 127 were assigned fluxes of 10.0 Jy, 29.0 Jy, 12.5 Jy, 6.5 Jy, and 19.2 Jy. Four cases are found where two 100 μm sources lie within the correlation radius of 90” around a 25 μm detection.

7. The 60 μm IRAS map

7.1. General remarks

For the 60 μm data, a smoother background allowed a final S/N of ≥ 4.5 as lower limit for the source detection, while all other settings – especially the lower surface brightness cutoff of 1.4 MJy/sr – remained unchanged. At this wavelength, numerous detections are not only found at the NE and SW ends of the bar, but also in the interconnecting regions, thereby tracing the overall shape of the main body of the SMC (Fig. 7, upper plot). Extended structures around the point-like source detections are also detected in the other regions, especially in the NE wing in the direction of the LMC (Fig. 7, lower row, left plot). The brightest regions, well isolated in the 12 μm and 25 μm maps, start to become connected by regions of lower luminosity. Numerous discrete sources are found as well.

7.2. Source catalog and classification

The number of extracted sources listed in Appendix C is 384, 124 of which reach flux densities of ≥ 1.0 Jy. Only these bright sources were used for further investigations. The number of sources identified with IRAS PSC/FSC sources or HII regions in former studies increases considerably: more than half of the sources (71) with flux densities ≥ 1.0 Jy are listed in the IRAS catalogs, 33 are classified as HII regions in the DEM sample. Finally, 84 of them fall into the general category “emission line star/emission object”. 95 of the brighter sources were classified as cold sources with $T_{\text{BB}} \leq 30$ K (“C” in our scheme), only 6 warm sources (“W”) were found. This means that nearly all relevant source detections above the flux limit are of cold origin. Even when compared to the 25 μm results, this number has nearly doubled (see Table 11). For 9 sources, a precise classification was not possible due to

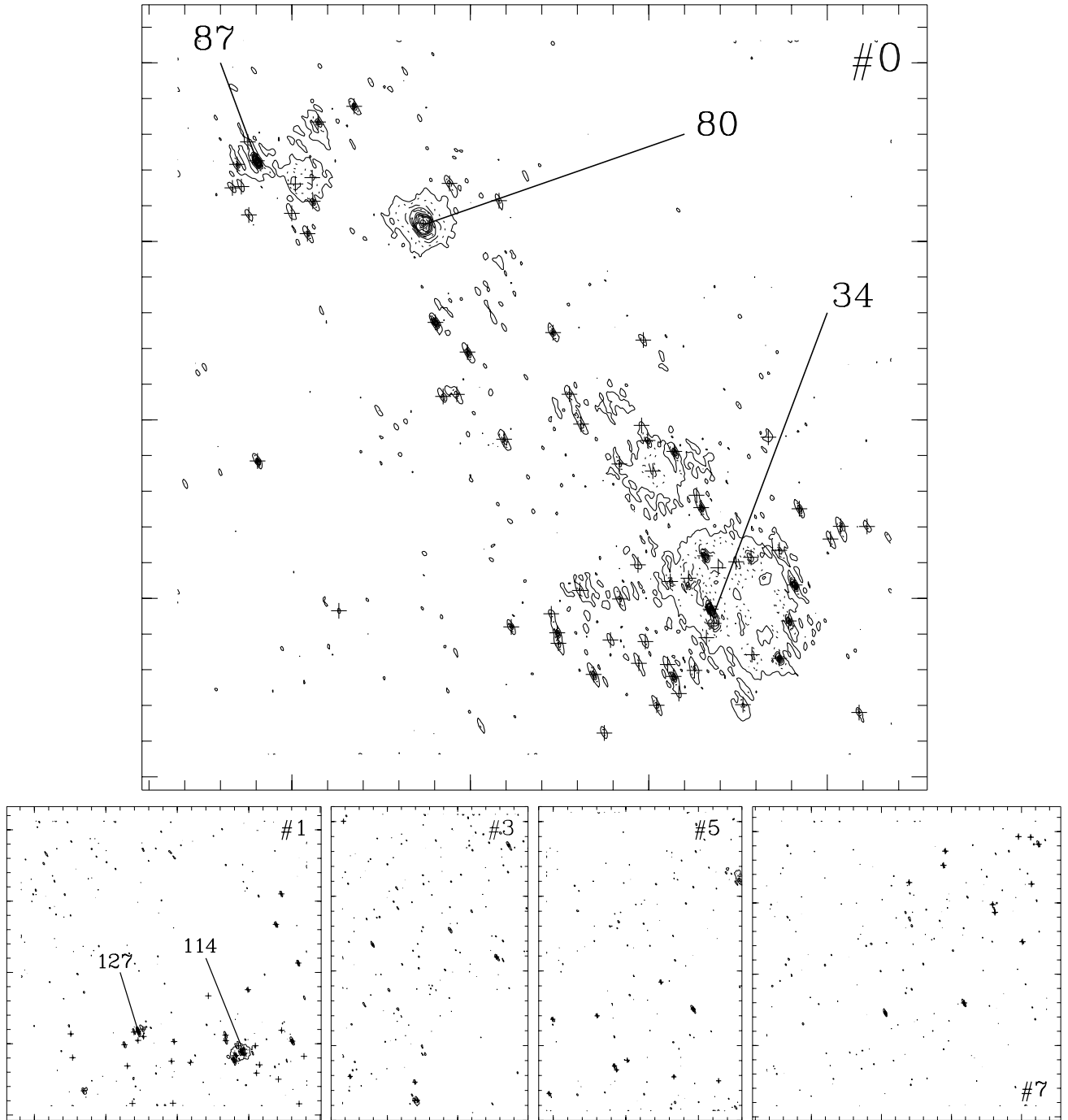


Fig. 6. $25\ \mu\text{m}$ IRAS HiRes data of the five examined SMC fields. Contours are plotted at the following flux levels: 1.8, 8, 16, 20, 28, 60, 120, 180 MJy/sr (solid lines), 3, 10, 20, 35, 80, 140, 200 MJy/sr (dotted lines), and 5, 12, 24, 40, 100, 160 MJy/sr (dashed lines). Upper contour plot: the central SMC field. Lower row, from left to right: adjacent SMC fields with numbers 1, 3, 5, and 7 in eastern, northern, western, and southern direction. As in Fig. 5, sources detected by HIIPhot are marked with a cross (+). Labelling numbers refer to the source entries in Appendix B.

missing wavelength bands, but they are assumed to be predominantly of type (C), due to their $170\ \mu\text{m}$ flux. Confusion with other sources in complementary wavelength bands affected the classification of 20 sources. Of 101 sources without $170\ \mu\text{m}$ identification, 75 exhibited $f_{100\ \mu\text{m}}/f_{60\ \mu\text{m}} \geq 1.0$, 26 were found with $f_{100\ \mu\text{m}}/f_{60\ \mu\text{m}} < 1.0$. The five landmark sources with numbers 79, 221, 271, 337, and 369 are assigned fluxes of 147.6 Jy, 283.2 Jy, 48.7 Jy, 79.2 Jy, and 56.6 Jy.

8. The $100\ \mu\text{m}$ IRAS map

8.1. General remarks

A lower S/N limit of 3.0 for the source detection yielded reasonable results. It allowed reliable source detection down to the outermost edges of the SMC with the weakest FIR emitting sources. Compared to the $60\ \mu\text{m}$ data a somewhat lower

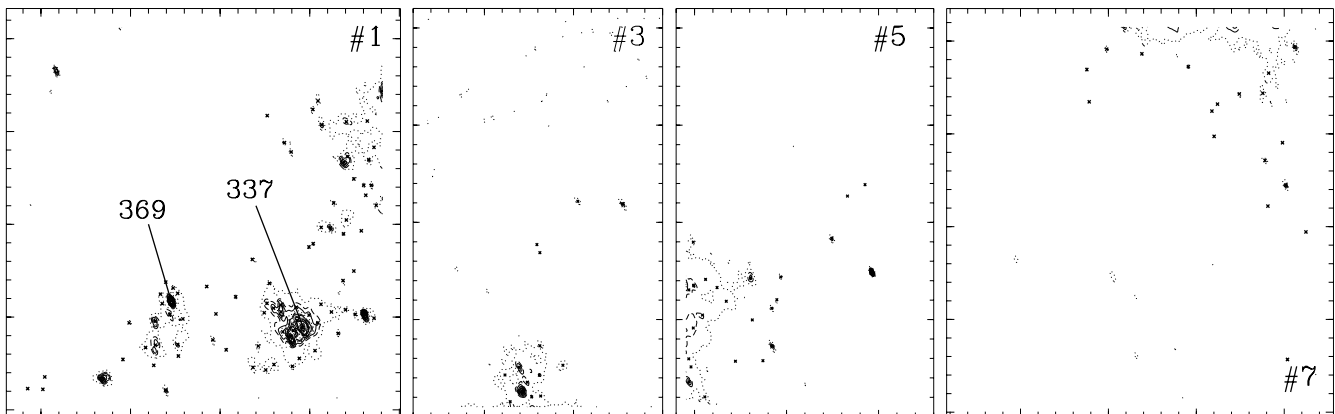
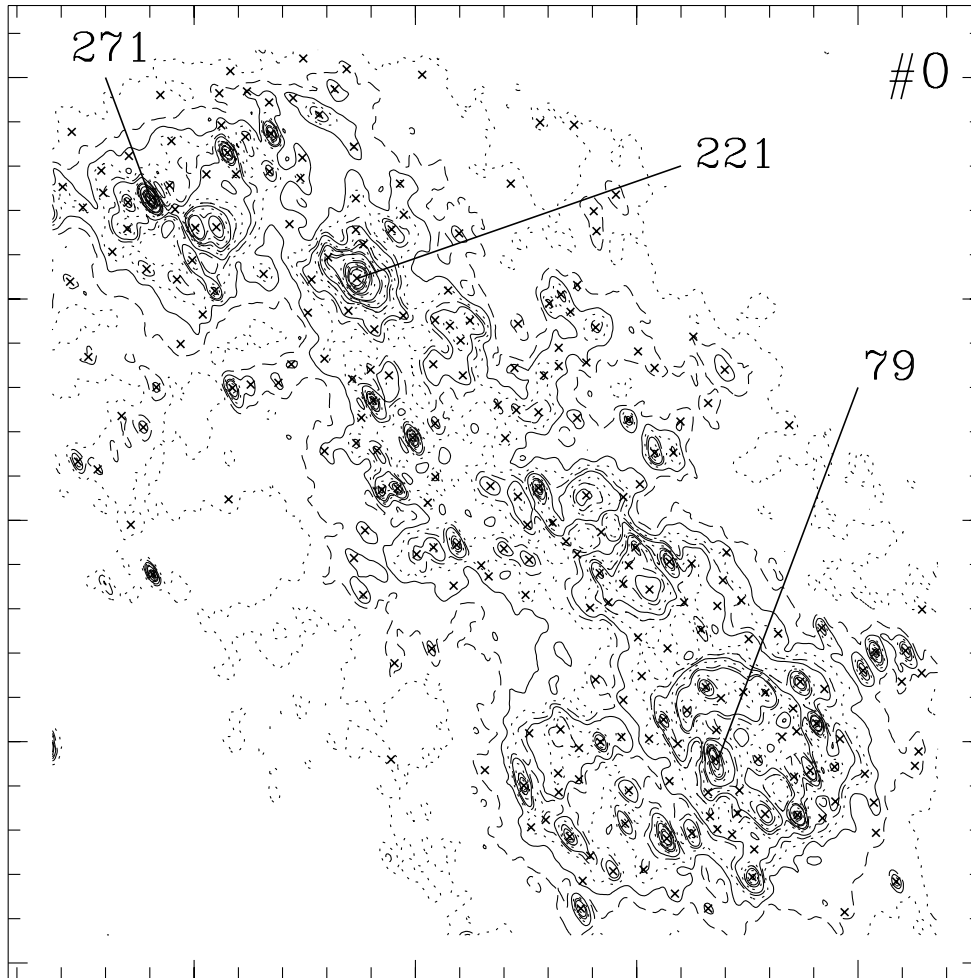


Fig. 7. 60 μm IRAS HiRes data of the five examined SMC fields. Contours are plotted at the following flux levels: 2, 8, 16, 20, 28, 60, 120, 180 MJy/sr (dotted line), 4, 10, 20, 35, 80, 140, 200 MJy/sr (dashed line), and 6, 12, 24, 40, 100, 160 MJy/sr (solid line). The plot order is the same as in Figs. 5 and 6. Different line types were chosen for the contours to illustrate the gradient, especially in the plateau-like regions. Sources found according to our detection criteria are marked with a cross (\times). Labelling numbers refer to the source entries in Appendix C.

number of sources is detected, comprising not only point-like sources with the highest flux densities but also extended ones with lower values. The source count differences are mainly due to the fact that the 100 μm map has a bigger PSF *FWHM* leading to a moderately reduced resolution. This is supported by the average distance between two neighbouring sources which is evidently larger at 100 μm (Fig. 8) than at 60 μm (Figs. 7).

At 100 μm , the SMC extends even further out than at 60 μm , the contours at the lower flux density levels suggest an overall homogeneous bar structure with significantly brighter regions in the NE and SW part and a few bright sources in between. Structures in the bridge region (Fig. 8, lower left plot) become more extended than at 60 μm (Fig. 7).

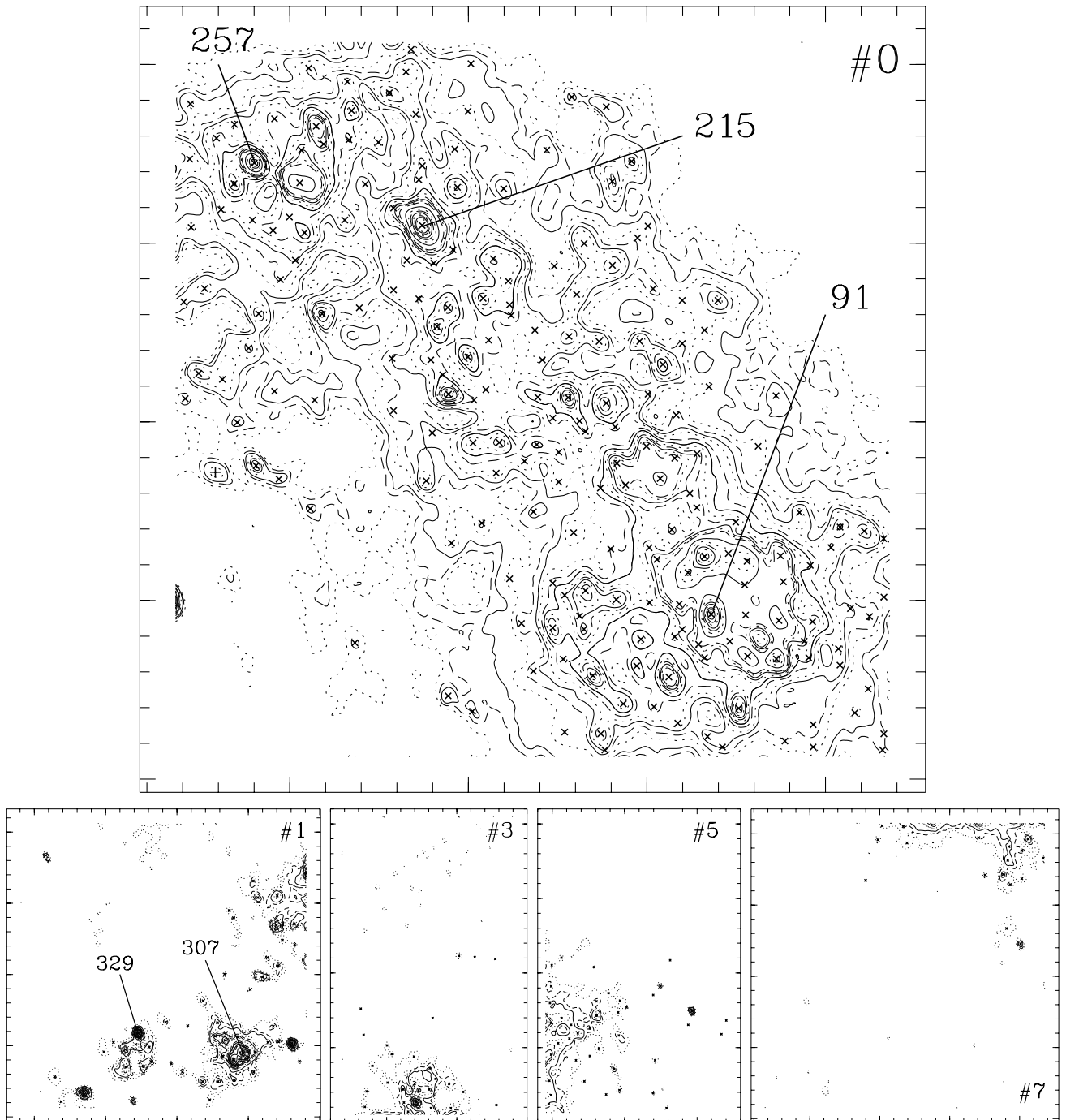


Fig. 8. $100\ \mu\text{m}$ IRAS HiRes data of the five examined SMC fields. Contours are plotted at the following flux values: 2, 6, 12, 24, 36, 80, 140, 200 MJy/sr (dotted line), 3, 8, 16, 20, 28, 40, 100, 160 MJy/sr (dashed line), and 4, 10, 20, 32, 60, 120, 180 MJy/sr (solid line). The plot order is the same as in Figs. 5–7. Different line types were chosen for the contours to illustrate the gradient, especially in the plateau-like regions. Sources found according to our detection criteria are marked with a cross (\times). Labelling numbers refer to the source entries in Table 5.

8.2. Source catalog and classification

The $100\ \mu\text{m}$ catalog comprises 338 sources in total (Appendix D). Most of the sources are assigned flux values of ≤ 5.0 Jy, however, a broad distribution spanning the range up to ≈ 40 Jy is seen in Fig. 17. Beyond that, only single sources are detected (similar to the $60\ \mu\text{m}$ case shown in Fig. 15). Five of the brightest sources labelled with numbers 91, 215, 257, 307,

and 329 in Fig. 8 were measured to 271.1 Jy, 330.0 Jy, 84.0 Jy, 178.6 Jy, and 58.4 Jy.

167 sources have flux density values ≥ 1.0 Jy and are used for further analysis. The remaining sources have the same properties as in the $170\ \mu\text{m}$ map (cf. following section): most of them are located in the outer regions of the SMC, far away from the more luminous HII regions along the major axis of the bar. Nearly all of them have low flux densities, too.

According to Table 4, 90 of the 167 luminous sources can be classified as “C”, the classification of 18 detections remains unclear due to source confusion between different wavelength bands. Of the sources of type “C”, 70 are found with $f_{170\mu\text{m}}/f_{100\mu\text{m}} \geq 1.0$, 16 with $f_{170\mu\text{m}}/f_{100\mu\text{m}} < 1.0$. These numbers are very similar to those found for the 60 μm catalog, although the percentage of cold sources shows a small decrease compared to the 60 μm case. Only 7 sources exhibit a spectrum with $T_{\text{BB}} \geq 30$ K, according to the classification criteria for our object class “W”. Among the sources which were not detected in the 170 μm band, the majority (57) exhibits flux ratios ($f_{100\mu\text{m}}/f_{60\mu\text{m}}$) above 1.0, some of them (22) also showed decreasing fluxes with increasing wavelengths ($f_{100\mu\text{m}}/f_{60\mu\text{m}} < 1.0$). The total number of objects as well as the distribution among the different object classes makes the 100 μm data directly comparable to the 60 μm and the 170 μm case. 63 of the 167 sources with $F_{\nu} \geq 1.0$ Jy are identified as IRAS sources from the PSC or FSC catalog, 22 of them are HII regions, and 70 of them fall into the category “emission line star/emission object”.

9. The 170 μm ISO map

9.1. General remarks

For the source detection in the ISO fields, the S/N value was fixed at ≥ 1.5 with all the other relevant computational parameters (e.g., the maximum source extension and the projected distance for the background estimation) remaining unchanged when compared to the IRAS cases.

The final map shown in Fig. 1 reveals a wealth of structure, not only along the bar of the SMC, but also in the direction of the Magellanic bridge, connecting the SMC to the LMC. The emission of the brightest HII regions (colored blue/white in Fig. 1) mainly originates from a ring-like structure in the southwestern part of the SMC, but also from isolated sources in the northeastern part of the bar. Three further bright HII regions are obviously located in the wing region. In the outer regions of the bar, numerous fainter sources (orange/red/yellow color) were found, which contribute significantly to the total FIR emission of the SMC.

Regarding the overall morphology of the SMC, the ISO map is rather similar to the 100 μm case: the main body of the SMC is traced well (as seen in Fig. 1), differences are visible in the outer part of the main SMC body and in the plateau regions of moderate surface brightness in the central SMC part along the major axis of the bar: at 170 μm , less sources are detected at low surface brightness values, so the bar appears wider at 100 μm .

9.2. Source catalog and classification

As given in Appendix E, a total number of 243 sources at 170 μm is detected of which 155 exhibit flux density values above 2.0 Jy. The remaining 88 weak sources were not taken into account for further studies, since most of them are basically cold clouds in the outer regions of the bar which do not

constitute the morphological structure (but nevertheless contribute to the integrated FIR emission).

The five sources labelled 16, 103, 135, 195, and 232 in Fig. 9 were assigned a growth luminosity of 453 Jy, 366 Jy, 198 Jy, 327 Jy, and 22 Jy, respectively (see table in Appendix E). 51 of the 155 bright sources were identified as IRAS PSC or FSC sources in the SIMBAD database, 99 were classified as cold sources (type “C”), 7 as warm (type “W”), and 19 remained unclassified (“Q”) due to obvious misclassification with other sources in the complementary wavelength bands. 30 source SEDs could not be classified due to missing flux density values at 100 μm or 60 μm , but are probably cold due to their high 170 μm value. 18 objects could be identified as HII regions from the DEM sample, 61 contributed to the “emission line star/emission object” category. For 74 of the sources the $f_{170\mu\text{m}}/f_{100\mu\text{m}}$ ratios are ≥ 1.0 , 16 have $f_{170\mu\text{m}}/f_{100\mu\text{m}}$ values < 1.0 . To summarize, the source extraction at 170 μm yields numerous new and formerly unknown cold FIR emitting sources which are not identified in other catalogs. Of the 155 brighter sources, 70 were assigned a general SED type (“W”, “C”, “(C)”). In addition, many of the sources classified as warm (“W”) in former studies were re-classified “C” by our study. This puts special emphasis on the importance of the 170 μm flux value in an SED of cold (< 30 K) objects for the determination of the blackbody temperature used for the dust emission models.

The basic properties of the 170 μm luminosity distribution given by the histogram in Fig. 10 are found to be the same as in the 60 μm and 100 μm cases: a large number of sources in the lowest flux bins (0.0 Jy ... 5.0 Jy) dominates the histogram distribution. On the other hand, single sources with very high luminosities are detected, ranging up to the 400 Jy level. Compared to the 100 μm data, the decrease in the total number of detections is of course caused by the considerably larger PSF F_{WHM} at 170 μm , making the separation of small adjacent sources difficult. Some 100 μm sources seem to be missing in the 170 μm observations. This is caused by the fact that the ISO 170 μm map does not cover the SW extension of the SMC with a few ten sources.

10. Cross-correlation of the catalogs

The statistics of a cross-correlation of the source catalogs in all five wavelength bands with each other are summarized in Table 4. The absolute number of cross-identified sources is given as well as the relative percentages. With the 170 μm source list as reference catalog, several conclusions can be drawn.

In general, the number of sources which are also detected at 170 μm increases considerably with increasing wavelength. E.g., while 45% to 47% percent of all sources found at 25 μm , 60 μm , and 100 μm are detected at 170 μm , this only holds for 29% of the 12 μm sources. Different dust heating mechanisms play a dominant role in producing the different appearance: While the 12 μm and 25 μm emission are dominated by ultrasmall grains which are subject to single-photon heating (Draine & Li 2001), the 100 μm through 170 μm emission is mostly produced by the emission of large grains of equilibrium

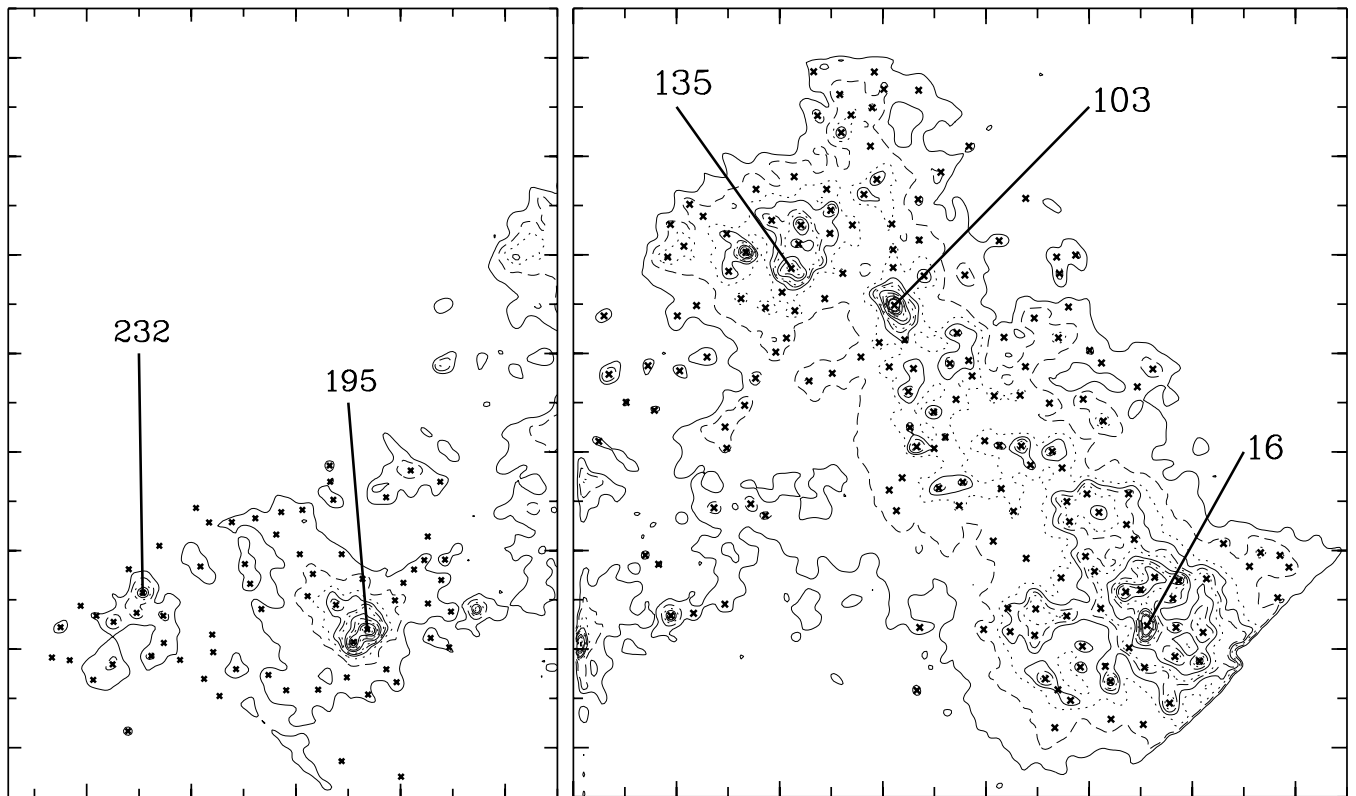


Fig. 9. ISO 170 μm data of the SMC, split up into two fields (for the subsequent comparison with the IRAS data). Contours are plotted at the following flux values: 0.1, 0.6, 1.4, 2.6, 3.8 Jy/pix (solid line), 0.2, 0.8, 1.8, 3.0, 4.2 Jy/pix (dashed line), and 0.4, 1.0, 2.2, 3.4 Jy/pix (dotted line). Different line types were chosen for the contours to illustrate the gradient, especially in the plateau-like regions. Sources found according to our detection criteria are marked with a cross (\times). Labelling numbers refer to the source entries in Table 6. Note that due to liquid helium boil off, the ISOPHOT observations do not cover the SMC to its full SW extent.

temperature. We also see different types of sources in the MIR (12 μm , 25 μm) and FIR (60 μm , 100 μm , 170 μm) bands. In the MIR, stars account for more than half of the entries already in the IRAS point source catalog (Beichmann 1987), with most of the emission coming from AGB stars with SEDs similar to those found in the papers by Groenewegen et al. (1999) or Fujii et al. (2002). Large numbers of these stars have been detected in the SMC already with their spectral properties being in good agreement with those found in our Galaxy (Zijlstra et al. 1996). These SEDs peak at 10 μm to 30 μm and there is no significant emission beyond 60 μm . The FIR emission is most likely dominated by HII regions with an SED peaking between 60 μm and 100 μm (Ghosh 2000) and molecular clouds.

Secondly, the two FIR IRAS maps (60 μm , 100 μm) and the 170 μm ISO map are closely related with respect to cross-identifications: of all ISO sources, more than 60% are identified at 60 μm and 100 μm as well, in addition, more than 45% of all 60 μm and 100 μm sources are found at 170 μm , too (see Table 4). This hints at a consistent source extraction for all three bands and suggests that most of the identified sources are physically connected. The fact that more than half of the 170 μm sources are not identified at 60 μm and 100 μm is mainly caused by different PSF sizes at the referring wavelengths, leading to different source morphologies and different center point positions for physically identical sources in different wavelength bands. At a cross-correlation radius of only 90'' as applied

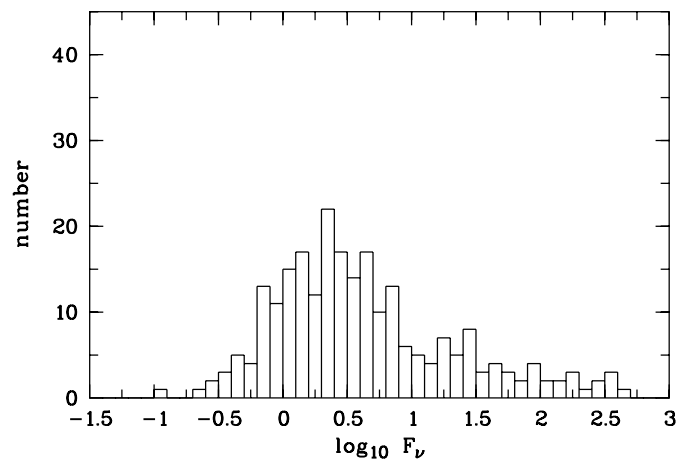


Fig. 10. Source distribution histogram for the 170 μm data. The decrease in number counts towards lower flux densities is caused by the S/N limit applied by the HIIPhot algorithm which rejects possible sources below this threshold.

by us (to avoid multiple identification pairs as far as possible), this means that many of them are regarded as independent ones when cross-correlating the catalogs. Finally, regarding cross-correlation, the 25 μm catalog not only resembles the other MIR IRAS case at 12 μm , but also seems to be connected to the FIR IRAS and ISO cases: the referring percentages for

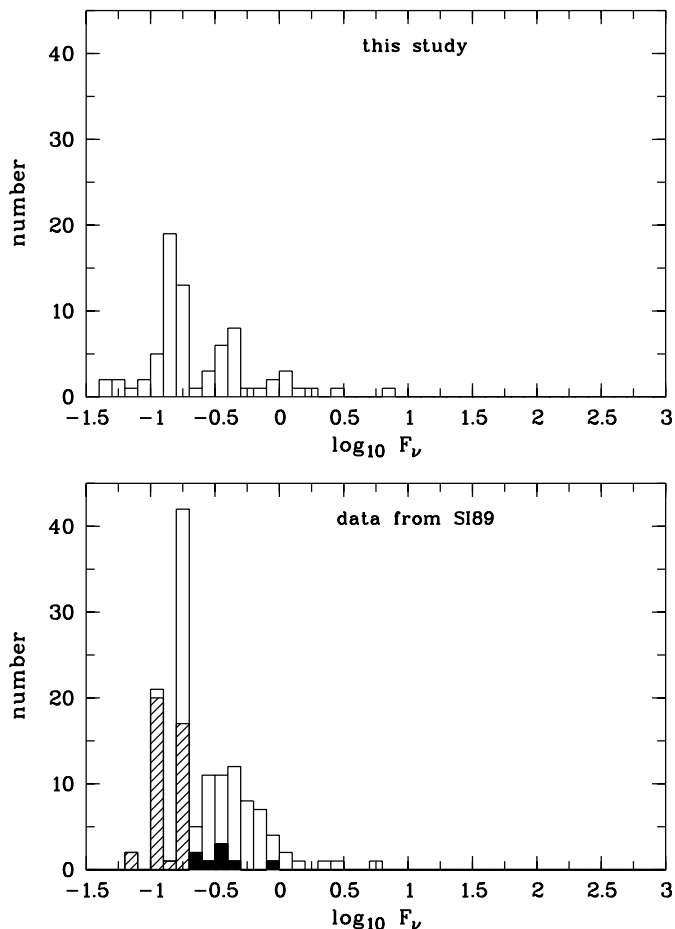


Fig. 11. $12\ \mu\text{m}$ source distribution histogram obtained for our study (upper panel) and SI89 (lower panel). Hatched areas in the SI89 plot indicate measurements with an uncertain flux value below $0.20\ \text{Jy}$. Black areas in the same plot represent uncertain results for fluxes $> 0.20\ \text{Jy}$. The total number $12\ \mu\text{m}$ sources in the flux bin $\log F_\nu = 0.8 \dots 0.9$ detected by our analysis method is smaller than in the SI89 study. The latter suffers from a large amount of uncertain results at the lowest flux levels as indicated by the hatched areas (lower plot), thereby affecting statistics in that flux region considerably.

cross-identification are nearly as high as those found for the $60\ \mu\text{m}$ case. One exception is found for the cross-correlation with the $12\ \mu\text{m}$ catalog, where 28% of the $25\ \mu\text{m}$ objects are identified at $12\ \mu\text{m}$, but only 8% for all three FIR wavelength bands at $60\ \mu\text{m}$, $100\ \mu\text{m}$, and $170\ \mu\text{m}$. So, interestingly enough, the $25\ \mu\text{m}$ results act as a kind of intermediate case between the $12\ \mu\text{m}$ results and the three FIR bands, although it is morphologically closely related to the $12\ \mu\text{m}$ map only.

11. Comparison with other catalogs

Figure 11 compares the flux distribution of our reliably detected $12\ \mu\text{m}$ sources (upper plot) with those given in the $12\ \mu\text{m}$ catalog in SI89. Both data sets show a similar luminosity distribution with the bulk of the sources below $0.2\ \text{Jy}$ and a few discrete sources with considerably larger values. Obviously, our algorithm detects less sources at very low intensities. Most of the faint sources found by SI89 were assigned a highly

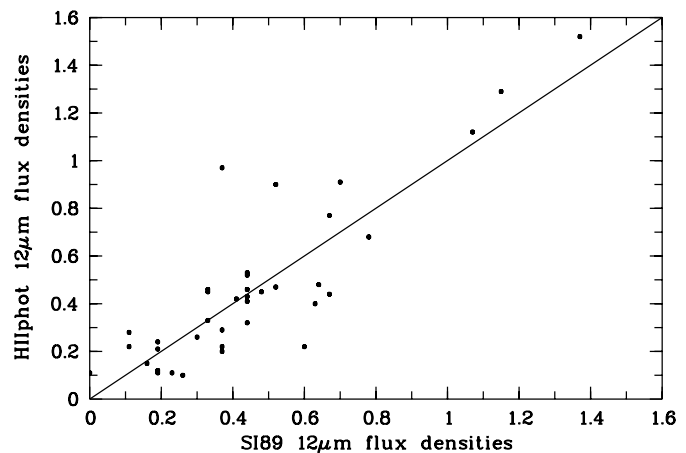


Fig. 12. Comparison of the $12\ \mu\text{m}$ fluxes of those sources that were commonly identified in our catalog from Appendix A and the catalog of SI89. Note that the total number of sources shown here is smaller than the entry list of both catalogs, since some of the SI89 sources were not detected by our routine and many of our detections were not listed in the SI89 catalogs before. The SI89 data appears binned in flux range (horizontal axis) due to the frequent occurrence of certain flux values in the referring tables (e.g., $0.19\ \text{Jy}$, $0.44\ \text{Jy}$). Evidently, statistics are poor for the whole luminosity range, so that no “average” behaviour of this data set can be derived. Sources with low fluxes ($< 0.6\ \text{Jy}$) tend to cluster around a flux ratio of 1.0, with a small excess towards lower HIIphot values, while brighter sources are assigned fluxes which are slightly higher than found in SI89. The small differences between this study and the SI89 results hint at the fact that a reliable estimation of the inhomogeneous background is essential for faint sources, a prerequisite which is difficult to achieve with the eyeball fitting method of SI89.

uncertain flux value which, in most cases, is very close to or identical with the detection limit in their IRAS maps.

Addressing the comparability of the SI89 results with ours, two questions have to be answered: i) how many sources are *commonly* detected in different wavelength bands and listed in the corresponding source catalogs, and ii) whether sources with different properties (luminosity, location in the SMC, background level/structure in their vicinity, etc.) are assigned different fluxes by the competing methods. To answer these questions, we directly compared our HIIphot IRAS source catalogs to those published in SI89 (see Fig. 12).

The faint detections (close to the zero point in Fig. 12) which are commonly identified in both $12\ \mu\text{m}$ catalogs tend to cluster roughly around the equality line, i.e., on average, our study and the SI89 method seem to assign identical source fluxes. However, statistics are poor due to the small total number of sources. A number of SI89 $12\ \mu\text{m}$ objects is not detected by our algorithm. Faint sources from our catalog ($< 0.5\ \text{Jy}$) tend to have slightly lower fluxes than the SI89 ones and therefore lie below the line $f_{\text{our study}}/f_{\text{SI89}} = 1$. Looking at the few brighter sources only, the situation seems different: the flux ratios tend to lie closer to one, and in addition, more sources tend to lie *above* the line $f_{\text{our study}}/f_{\text{SI89}} = 1$, i.e., our growth provides us with higher final fluxes than found in the SI89 catalog.

For the $25\ \mu\text{m}$ source list, the situation is similar: in general, our luminosity distribution and source counts (Fig. 13, upper

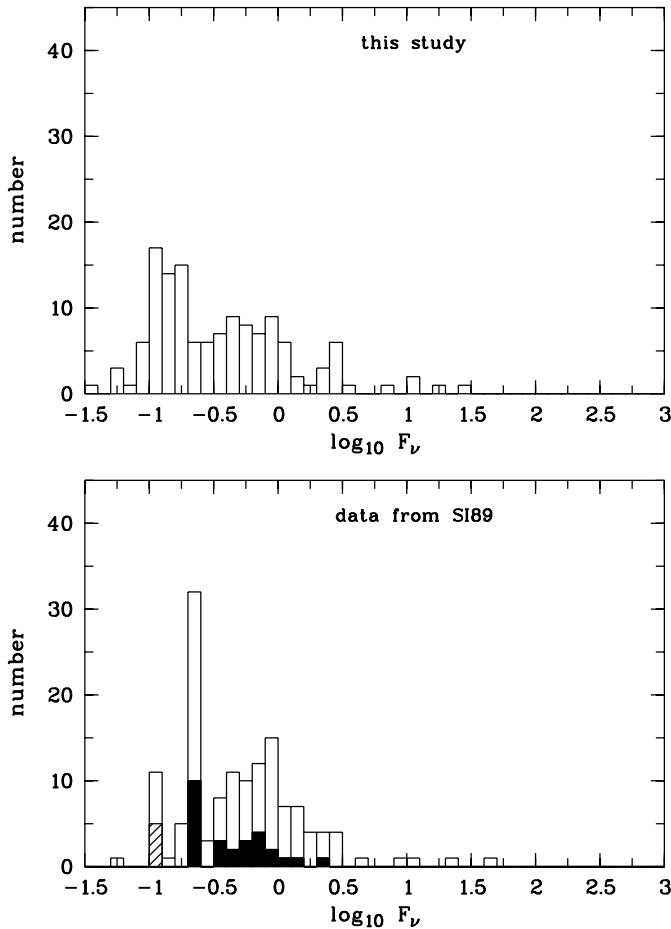


Fig. 13. Distribution histogram for the $25\ \mu\text{m}$ IRAS sources found by this study (upper plot) and the ones from SI89 (lower plot). Note the different y -axis-scaling. As in Fig. 11, hatched and black areas in the SI89 plot (lower panel) indicate uncertain results for fluxes ≤ 0.20 Jy and > 0.20 Jy, respectively. The source luminosity distributions are similar – though not identical – in both samples, with a tendency to more sources with comparably low luminosities in our database. Compared to the $12\ \mu\text{m}$ case in Fig. 11, less uncertain flux values are contained in the SI89 histogram. The total number of detections are comparable in both studies.

plot) resemble very much those of SI89 (lower plot). The only difference is that we detect slightly less sources in the luminosity bin $1.0\ \text{Jy} \dots 2.0\ \text{Jy}$. For large luminosities ($\geq 6\ \text{Jy}$), statistics become poor in both cases, so a reliable comparison of both data sets in this flux regime is not possible.

Regarding the comparison of the fluxes assigned by HIIphot and the SI89 study (Fig. 14), it is obvious that many more sources of low luminosity than in the $12\ \mu\text{m}$ case are commonly identified in the two different $25\ \mu\text{m}$ catalogs, providing us with better statistics. The $25\ \mu\text{m}$ results are very similar to the $12\ \mu\text{m}$ ones: for fainter sources ($< 1.5\ \text{Jy}$), our study and the SI89 results are in very good agreement, brighter sources are again assigned slightly higher values in our study.

Addressing number counts and cross-correlation with other catalogs, major changes occur at $60\ \mu\text{m}$: the overall number of reliable detections rises considerably to 384, which is the largest value of all catalogs/wavelength bands considered here.

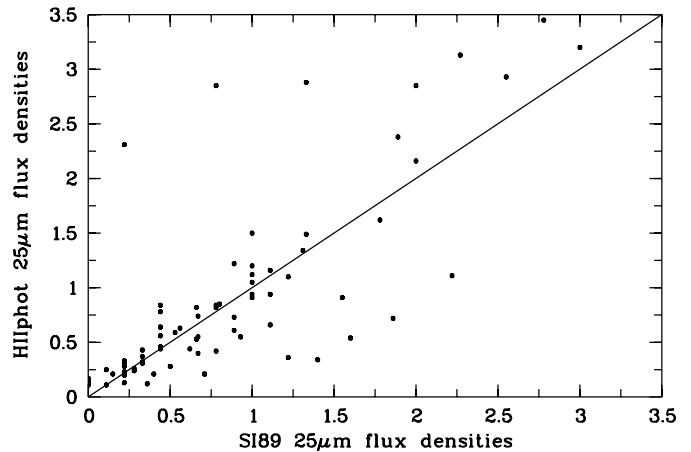


Fig. 14. Comparison of the $25\ \mu\text{m}$ flux ratio distribution of those sources commonly identified in our catalog and the one presented in SI89. Note that the total number of sources shown here is much smaller than the entry list of both catalogs. The SI89 data appears binned in flux range (horizontal axis) due to the frequent occurrence of certain flux values in the referring tables (e.g., $0.22\ \text{Jy}$, $0.44\ \text{Jy}$, $1.00\ \text{Jy}$). On average, the HIIphot algorithm assigns similar fluxes to fainter sources ($< 1.7\ \text{Jy}$), yielding a good correlation between our results and the values given in SI89. Brighter and very bright sources ($> 1.7\ \text{Jy}$) predominantly populate regions above the line $f_{\text{our study}}/f_{\text{SI89}} = 1$.

But while the analysis performed in SI89 yields only 68 sources with fluxes up to $2.5\ \text{Jy}$, our list in Appendix C contains 291 discrete sources at the same flux level. Evidently, our detection algorithm is well capable of detecting low-flux sources even in crowded regions of the main body of the SMC. According to the data presented in SI89, a broad source distribution extends up to fluxes of $\approx 20\ \text{Jy}$. Beyond that, only single sources are detected in each flux bin (see Fig. 15, lower plot). In this flux regimes, statistics become poor, so a comparison between the two methods does not make any sense anymore.

In general, the source flux comparison of the $60\ \mu\text{m}$ catalog with the SI89 data set shown in Fig. 16 (upper and lower plot) yields results which slightly differ from those found for the $25\ \mu\text{m}$ data (Fig. 14): faint sources ($< 10\ \text{Jy}$) now lie distinctly below the line $f_{\text{our study}}/f_{\text{SI89}} = 1$ and exhibit a large scatter for all flux values up to $10\ \text{Jy}$. Similar to the $12\ \mu\text{m}$ and $25\ \mu\text{m}$ case, brighter sources with fluxes up to $\approx 160\ \text{Jy}$ tend to lie above the equality line. But since statistics are better now for the compared $60\ \mu\text{m}$ catalogs, it is evident that the HIIphot fluxes do not approach the SI89 ones, even not for the highest flux regime. This may be a result of the automated growth procedure down to a surface brightness threshold of $1.4\ \text{MJy/sr}$ which collects more flux than a visual method (depending on background structure and source morphology).

Figure 17 shows the superior performance of the HIIphot algorithm: while SI89 lists only 45 sources for the $100\ \mu\text{m}$ case in the interval $0.0\ \text{Jy} \dots 5.0\ \text{Jy}$, we find more than five times as many of them (272). The SI89 results suffer from source confusion preventing the identification and the precise flux determination of a large number of sources. Their catalog lists 79 cases of non-identifications due to source confusion,

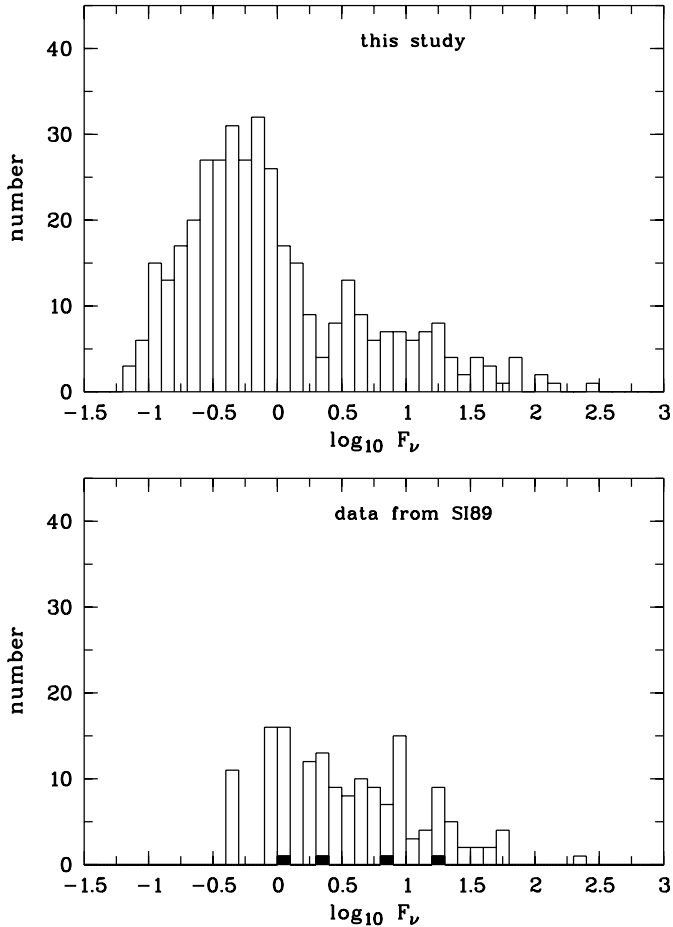


Fig. 15. Distribution histogram for the $60\ \mu\text{m}$ IRAS sources found by this study (upper plot) and the ones from SI89 (lower plot). Black areas in the lower plot indicate uncertain measurements. The source #221 with a flux of 283.2 Jy is not included in the plot. Evidently, our analysis produces a huge number of additional sources at low and very low luminosity values. In addition, several sources with $F_\nu \geq 60$ Jy are detected which are not found in the analysis of SI89.

a subset which is well detected by our extraction code. Most of these sources populate the flux regions <3.0 Jy where SI89 sources are nearly completely missing. In addition, our $100\ \mu\text{m}$ catalog (Appendix D) also contains a number of sources with fluxes ≥ 60 Jy which tend to be brighter than found by SI89. These sources lie in the vicinity of crowded FIR emitting regions, so it can be assumed that our method allows for a more reasonable background estimation in strongly emitting areas. For source fluxes <20.0 Jy, the HIIphot fluxes at $100\ \mu\text{m}$ lie below the SI89 ones which exhibit a considerable scatter (Fig. 18). For more luminous sources, the HIIphot fluxes exceed the SI89 ones, which makes our $100\ \mu\text{m}$ results directly comparable to the $60\ \mu\text{m}$ case.

To summarize, all four revisited IRAS source catalogs behave remarkably similar when compared to the corresponding results given in SI89: faint sources tend to be assigned lower flux densities in our study, and bright sources (depending on the wavelength) sometimes have considerably larger flux values than found by SI89. This is the result of mainly two

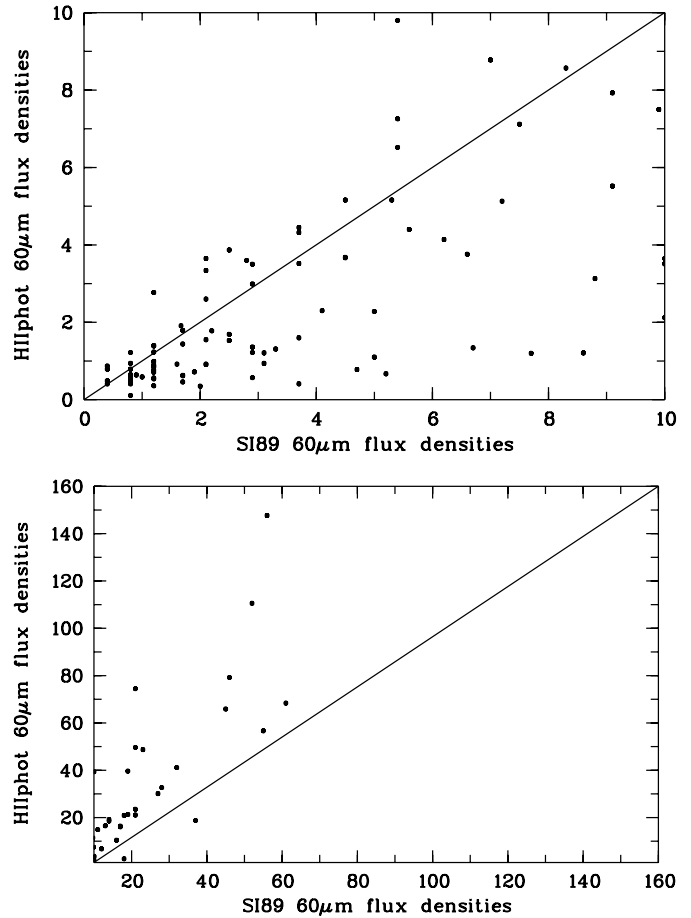


Fig. 16. Comparison of the $60\ \mu\text{m}$ flux densities of those sources that were commonly identified in our data and the catalog of SI89 for faint (upper plot) and bright sources (lower plot). Note that the total number of sources shown here is much smaller than the entry list of both catalogs due to the same reasons as given in Figs. 12 and 14. Especially the majority of our detections below 1 Jy had not been detected by the SI89 method before. The SI89 data appears binned in flux range (horizontal axis) due to the frequent occurrence of certain flux values in the referring tables (e.g., 1.2 Jy, 0.8 Jy). Compared to the SI89 results, our sources tend to be assigned higher fluxes in the case of brighter sources (>10 Jy) and lower values for fainter ones.

interfering effects which apply to sources of low *and* high luminosities which lie in different regions of the SMC:

- On the one hand, our program, due to its growth procedure, assigns higher flux values to cases where the manual fitting procedure underestimates the extension of the source luminosity profile down to low-flux areas. This predominantly affects comparably bright sources in all bands which are located on a high background level and where the footpoints of the luminosity profile are difficult to detect with eyeball fitting methods;
- On the other hand, a background overestimated by eyeball fitting procedures may not be reliably established especially in crowded regions. Depending on the background level and structure in the vicinity of an extended source, this leads to partially lower or higher flux values. Especially for faint sources, a precise background subtraction plays an

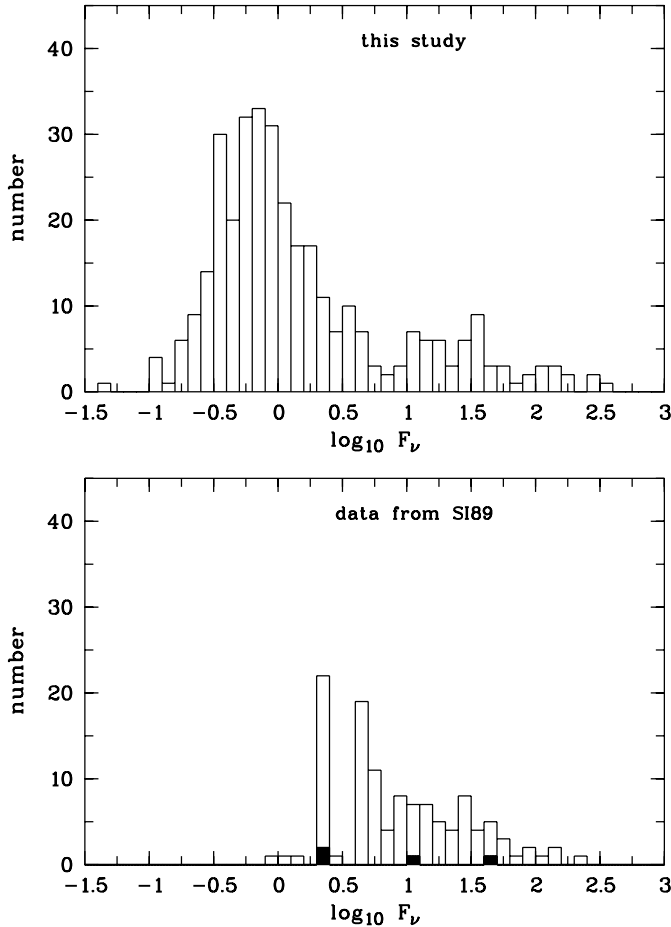


Fig. 17. Distribution histogram for the $100\ \mu\text{m}$ sources found by our study (upper plot) and the ones from SI89 (lower plot). Note the different y -axis-scaling. Black columns in the lower panel indicate uncertain flux values. In contrast to the results of SI89, large numbers of sources are detected, also at low luminosities. At the same time, the brightest sources from our analysis appear even brighter than was found by SI89.

essential role. Since the Schwering and Israel study yields higher values for, e.g., most of the $12\ \mu\text{m}$ fluxes, they probably underestimated the contribution from the substantially inhomogeneous background to the total flux for most of the faint sources.

We do not conform to the statement in the SI89 paper that a visual inspection of the background around each individual source yields better results than an automated program, especially when taking into account possible differences between empty regions (in the outer part of the SMC) and crowded ones (along the bar of the SMC) where a visual inspection nearly always fails.

12. Conclusion

In this paper we present a complete map of the SMC at $170\ \mu\text{m}$ with good S/N values even in the outer parts, and an excellent spatial resolution fully comparable to those of the $60\ \mu\text{m}$ and $100\ \mu\text{m}$ HiRes IRAS maps.

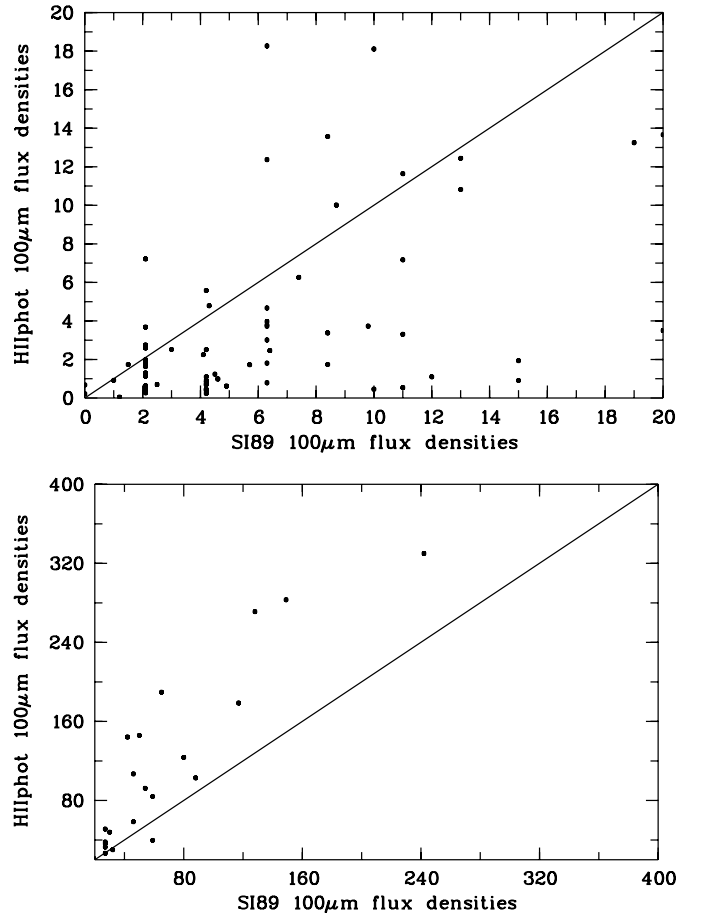


Fig. 18. Comparison of the $100\ \mu\text{m}$ flux ratio distribution of those sources that were commonly identified in our analysis and the catalog of SI89. Upper plot: low fluxes, lower plot: high fluxes. The diagonal is defined by $flux_{\text{our study}}/flux_{\text{SI89}} = 1$. The SI89 data appears binned in flux range (horizontal axis) due to the frequent occurrence of certain flux values in the referring tables (e.g., 2.1 Jy, 4.2 Jy, 6.3 Jy). Our study tends to assign considerably higher fluxes for the brighter sources than did the SI89 study, while the fainter objects are assigned lower values. In general, the $100\ \mu\text{m}$ case is very similar to the $60\ \mu\text{m}$ case (Fig. 16).

The ISO and the four IRAS HiRes maps were analysed using a new computational method of detecting sources and determining source fluxes. It turned out that the HIIPHOT algorithm leads to an accurate and reproducible photometric characterization of the SMC. Overlapping sources in crowded fields were equally well detected as weak extended sources in regions of an inhomogeneous background. Since the ISOPHOT data from the ISO archive and the four IRAS data sets from the IPAC IRAS archive were treated in an identical manner, this allowed for a direct comparison between the ISO and the (older) IRAS data.

Data sets were studied using the automated HIIPHOT algorithm for localizing point-like and extended MIR and FIR sources. Fluxes were derived and used to generate source catalogs for every wavelength band which are complete down to a detection limit which is given by the final surface brightness value where the source growth stops. A cross-correlation between the resulting catalogs was performed to identify

Table 4. Comparison between the ISO and the IRAS statistical results from our analysis. *: if a lower flux limit applies (e.g., sources with flux densities >1.0 Jy or 2.0, as given in the third line from top), numbers refer to the selected flux range only.

data set	ISO 170 μm	IRAS 12 μm	IRAS 25 μm	IRAS 60 μm	IRAS 100 μm
Appendix	E	A	B	C	D
$n_{\text{source total}}$	243	73	135	384	338
	155 with $F_{\nu} > 2.0$			124 with $F_{\nu} > 1.0$	167 with $F_{\nu} > 1.0$
cross-id. 170 μm	—	21 (29%)	61 (45%)	180 (47%)	162 (48%)
cross-id. 12 μm	20 (8%)	—	38 (28%)	31 (8%)	27 (8%)
cross-id. 25 μm	56 (23%)	36 (49%)	—	88 (23%)	71 (21%)
cross-id. 60 μm	153 (63%)	29 (40%)	90 (67%)	—	130 (68%)
cross-id. 100 μm	156 (64%)	26 (36%)	76 (56%)	234 (61%)	—
F_{ν} range [Jy]	0.3...450	0.1...1.0	0.06...3.0	0.06...25	0.08...160
$F_{\nu, \text{landmarks}}$ [Jy]	453/366/198/327/22	1.1/1.1/1.5/0.9/1.7	10.0/29.0/12.5/6.5/19.2	148/283/48/79/57	271/330/84/179/58
n_{C}	99* (64%*)	18 (25%)	41 (30%)	95* (77%*)	90* (54%*)
n_{W}	7* (5%*)	3 (4%)	6 (4%)	6* (5%*)	7* (4%*)
n_{Q}	19* (12%*)	—	9 (7%)	9* (7%*)	18* (11%*)
$f_{170}/f_{100} > 1$	74* (48%*)	2 (3%)	24 (18%)	—	70* (42%*)
$f_{170}/f_{100} < 1$	16* (10%*)	2 (3%)	12 (9%)	—	16* (10%*)
$f_{100}/f_{60} > 1$	—	—	—	75* (60%*)	57* (34%*)
$f_{100}/f_{60} < 1$	—	—	—	26* (21%*)	22* (13%*)
$n_{\text{IRAS sources}}$	51* (33%*)	25 (34%)	60 (44%)	71* (57%*)	63* (38%*)
$n_{\text{HII regions}}$	18* (12%*)	14 (19%)	31 (23%)	33* (27%*)	22* (13%*)
$n_{\text{ELS/EMO}}$	61* (40%*)	38 (52%)	79 (59%)	84* (68%*)	70* (42%*)
$N_{\text{SI89, NOT id.}}$	—	69%	41%	35%*	31%*

Entries in column #1 are defined as follows:

$n_{\text{source total}}$:	total number of detected sources in each band.
cross-id. xxx μm :	number of sources cross-identified in the xxx μm catalog.
F_{ν} range [Jy]:	flux density range covered by most of the sources.
$F_{\nu, \text{landmarks}}$ [Jy]:	flux densities of five sources which were identified in all five bands via cross-correlation of the catalogs, therefore serving as landmarks.
n_{C} :	number of sources classified as cold (“C”, meaning $T_{\text{BB}} < 30$ K for $\beta = 2$) [*] .
n_{W} :	number of sources classified as warm (“W”, meaning $T_{\text{BB}} > 30$ K for $\beta = 2$) [*] .
n_{Q} :	number of sources which could not be classified “W” or “C” due to source confusion between different wavelength bands [*] .
$f_{170}/f_{100} > 1$:	number of sources with a f_{170}/f_{100} flux ratio >1 [*] .
$f_{170}/f_{100} < 1$:	number of sources with a f_{170}/f_{100} flux ratio <1 [*] .
$f_{100}/f_{60} > 1$:	same as above, but for the f_{100}/f_{60} flux ratio [*] .
$f_{100}/f_{60} < 1$:	same as above, but for the f_{100}/f_{60} flux ratio [*] .
$n_{\text{IRAS sources}}$:	number of sources identified as IRAS Point Source Catalog (PSC) or Faint Source Catalog (FSC) objects in SIMBAD [*] .
$n_{\text{HII regions}}$:	number of sources identified as HII regions in the paper of Davies et al. (1976).
$n_{\text{ELS/EMO}}$:	number of sources classified as emission line star or emission object [*] .
$N_{\text{SI89, NOT id.}}$:	number of sources found by SI89 which could NOT be recovered in our analysis [*] .

identical sources. Differences between our analysis and former studies could be quantified, statistical results are summarized and presented in Table 4.

The following statements can be made:

1. The 170 μm ISO map of the SMC reveals a wealth of structure, not only consisting of filamentary FIR emitting regions, but also of numerous (243 in total) bright sources with fluxes up to ≈ 450 Jy which trace the bar along its

major axis as well as the bridge which connects the SMC to the LMC.

2. Our 170 μm ISO data set enables us to perform a general classification of the SEDs of the detected sources. According to Table 4, most of the brighter ISO sources (>2.0 Jy) are cold. We detected:
 - 99 sources, mostly associated with molecular clouds, with a cold spectrum (labelled “C”, with $T_{\text{BB}} < 30$ K).

- 70 of them are assigned a general SED type for the very first time.
- 7 warm sources ($T_{\text{BB}} > 30$ K), predominantly HII regions.
 - 19 objects where the classification remains unclear due to source confusion.
3. Most compact sources with reliably determined fluxes are already detected in the MIR wavelength range (73 at $12\ \mu\text{m}$ and 135 at $25\ \mu\text{m}$), although the MIR IRAS data is not capable of shedding much light on the complex morphological structure of the SMC main body. The source fluxes predominantly lie below 1.0 Jy.
 4. The $60\ \mu\text{m}$ and $100\ \mu\text{m}$ FIR IRAS and the ISO map of the SMC were found to be closely correlated by
 - tracing the overall morphology of the SMC main body, the bridge and the wing in a similar manner and
 - producing similar source counts with hundreds of sources (243 to 384, depending on the FIR band) with comparable luminosity distributions.
 5. The integrated source counts of the three FIR maps are dominated by the large contribution of low-luminosity objects <1 Jy ($60\ \mu\text{m}$ and $100\ \mu\text{m}$ IRAS data) or <2 Jy (ISO $170\ \mu\text{m}$ map), which have not been detected before. The distribution of very bright sources remains almost unchanged.
 6. It is evident from the flux distributions that the HIIphot algorithm confirms the general results for the $12\ \mu\text{m}$ and $25\ \mu\text{m}$ bands obtained in the SI89 study and produces comparable source numbers and flux distributions for both, luminous and fainter sources.
 7. Our $60\ \mu\text{m}$ and $100\ \mu\text{m}$ results strongly differ in number counts and luminosity distributions from those found in previous studies. Compared to the SI89 results, the HIIphot algorithm usually assigns lower fluxes to faint sources and higher or similar fluxes to bright ones. Since most of the bright sources are located in crowded regions on a high background level, this demonstrates that the automated algorithm is superior of detecting weak sources in crowded SMC fields and performing a reliable background subtraction in low- and high-intensity fields at the same time.
 8. Two different and competing processes are likely to explain differences in the sources fluxes of this and of earlier studies:
 - The background level determination can differ from those estimated by eyeball-fitting procedures (depending on the source and its surroundings).
 - The HIIphot growth procedure, taking into account even the faintest part of the luminosity profile of a source, may work in the same direction, since for visual inspection the tendency of underestimating the real source extension is high.
 9. Adjacent sources are disentangled unambiguously by our source extraction algorithm. A remarkable result is that numerous sources listed in the SI89 data set were NOT found by our method. This does not only affect faint sources with luminosities slightly above the detection limit, but even occurs for sources with SI89 flux densities up to 45 Jy. In detail, 69% ($12\ \mu\text{m}$), 41% ($25\ \mu\text{m}$), 35% ($60\ \mu\text{m}$), and 31%

($100\ \mu\text{m}$) of the sources identified by SI89 were not found by our study. The exact reason for that remains unknown, however, discrepancies have been reported several times already, e.g., by Filipovic et al. (1998b). Since the SI89 catalog was generated using eyeball fitting methods, we believe that the results presented here are a more reliable base for crosscorrelation with other spectral regimes.

Acknowledgements. This work was performed at the ISOPHOT Data Centre at MPIA which is supported by Deutsches Zentrum für Luft- und Raumfahrt e.V. (DLR) with funds of Bundesministerium für Bildung und Forschung, grant 50QI0201, the Max-Planck-Gesellschaft, and ESA funds supporting the scientific data reduction. This research has made use of the Simbad Database, operated at CDS, Strasbourg, France, and NASA's Astrophysics Data System Abstract Service. The authors would like to thank D.Thilker for publishing his code in the internet and thereby making it accessible for an interested public.

References

- Assendorp, R., Bontekoe, T. R., de Jonge, A. R. W., et al. 1995, *A&AS*, 110, 395
- Ardeberg, A., & Maurice, E. 1977, *A&AS*, 30, 261
- Azzopardi, M., & Vigneau, J. 1982, *A&AS*, 50, 291
- Aumann, H. H., Fowler, J. W., & Melnyk, M. 1990, *AJ*, 99, 1674
- Beichmann, C. A. Neugebauer, G. Habing, H. J. Clegg, P. E. & Chester, T. J. 1985, *IRAS Catalogs and Explanatory Supplement*, JPL D-1855
- Beichmann, C. A. 1987, *ARA&A*, 1987, 25, 521
- Bontekoe, T. R., Koper, E., & Kester, D. J. M. 1994, *A&A*, 284, 1037
- Bruhweiler, F. C., Klingensmith III, D. A., Gull, T. R., & Sofia, S. 1987, *ApJ*, 317, 152
- Caplan, J., Taisheng, Y., Deharveng, L., Turtle, A. J., & Kennicutt, R. C. 1996, *A&A*, 307, 403
- Cioni, M.-R., Loup, C., Habing, H. J., et al. 2000, *A&AS*, 144, 235
- Davies, R. D., Elliot, K. H., & Meaburn, J. 1976, *MNRAS*, 81, 89D (DEM)
- Draine, B. T., & Li, A. 2001, *ApJ*, 551, 807
- Filipović, M. D., Jones, P. A., White, G. L., et al. 1997, *A&AS*, 121, 321
- Filipović, M. D., Pietsch, W., Haynes, R. F., et al. 1998, *A&AS*, 127, 119
- Filipović, M. D., Jones, P. A., White, G. I., & Haynes, R. F. 1998, *A&AS*, 130, 441
- Fujii, T., Nakada, Y., & Parthasarathy, M. 2002, *A&A*, 385, 884
- Gabriel, C., Acosta-Pulido, J., Heinrichsen, I., et al. 1997, *Astronomical Data Analysis Software and Systems VI*, ed. G. Hunt, & H. E. Payne, ASP Conf. Ser., 125, 108
- Ghosh, S. K., *BASI*, 2000, 28, 225
- Gotthelf, E. V., Hamilton, T. T., & Helfand, D. J. 1996, *ApJ*, 466, 779
- Groenewegen, M. A. T., Baas, F., Blommaert, J. A. D. J., et al. 1999, *A&AS*, 140, 197
- Haberl, F., Filipović, M. D., Pietsch, W., & Kahabka, P. 2000, *A&AS*, 142, 41
- Haynes, R. F., Klein, U., Wayte, S. R., et al. 1991, *A&A*, 252, 475
- Helou, G., & Walker, D. W. (eds.), *IRAS Small Scale Structure Catalog*, JPL D-2988
- Henize, K. G. 1956, *ApJS*, 2, 315
- Hook, R., Lucy, L., Stockton, A., & Ridgway, S. 1994, *ST-ECF Newsletter*, 21, 16

- Hook, R. N., & Fruchter, A. S. 1997, *Astronomical Data Analysis Software and Systems VI*, ed. G. Hunt, & H. E. Payne, ASP Conf. Ser., 125, 147
- Hook, R. N., & Fruchter, A. S. 2002, *PASP*, 114, 144
- Inoue, H., Koyama, K., & Tanaka, Y. 1983, *IAUS*, 535
- Israel, F. P., Johansson, L. E. B., Lequeux, J., et al. 1993, *A&A*, 276, 25
- Kalluri, S., & Arce, G. R. 1998, *IEEE Trans. Signal Proc.*, 46, 322
- Klaas, U., Haas, M., Müller, S. A. H., et al. 2001, *A&A*, 379, 823
- Kessler, M. F., Steinz, J. A., Anderegg, M. E., et al. 1996, *A&A*, 315, L27
- Laureijs, R. J., Klaas, U., Richards, P. J., Schulz, B., & Ábrahám, P. 2000, *The ISO Handbook, Volume V: PHT - The Imaging Photopolarimeter, Version 1.1*, SAI/99-069/dc
- Lemke, D., Klaas, U., Abolins, J., et al. 1996, *A&A*, 315, L64
- Lequeux, J., Le Bourlot, J., Pineau des Forêts, G., et al. 1994, *A&A*, 292, 371
- Martin, N., Maurice, E., & Lequeux, J. 1989, *A&A*, 215, 219
- Meyssonnier, N., & Azzopardi, M. 1993, *A&AS*, 102, 451
- Murai, T., & Fujimoto, M. 1980, *PASJ*, 32, 581
- Putman, M. E., Gibson, B. K., & Staveley-Smith, L. 1998, *Nature*, 394, 752
- Rowan-Robinson, M. 1986, *MNRAS*, 219, 737
- Rubio, M., Lequeux, J., & Boulanger, F. 1993, *A&A*, 271, 9
- Sasaki, M., Haberl, F., & Pietsch, W. 2000, *A&AS*, 147, 75
- Schlegel, D. J., Finkenbeiner, D. P., & Davis, M. 1998, *AJ*, 500, 525 (SFD)
- Schwering, P. B. W., & Israel, F. P. 1989, *A&AS*, 79, 79 (SI89)
- Stanimirovic, S. 1999, Ph.D. Thesis, University of Western Sydney Nepean
- Stanimirovic, S., Staveley-Smith, L., van der Hulst, J. M., et al. 2000, *MNRAS*, 315, 791
- Staveley-Smith, L., Sault, R. J., Hatzidimitriou, D., Kesteven, M. J., & McConell, D. 1997, *MNRAS*, 289, 225
- Sternberg, S. 1986, *Computer Vision, Graphics and Image Processing* 35, 333
- Stetson, P. B. 1987, *PASP*, 99, 191
- Stetson, P. B. 1994, *PASP*, 106, 250
- Thilker, D. A., Braun, R., & Walterbros, R. A. M. 2000, *AJ*, 120, 3070
- Thronson, H. A. Jr., & Shull, J. M. 1989, *The Interstellar Medium in Galaxies, Second Wyoming Conference, USA* (Kluwer Academic Publishers), 483
- Tumlinson, J., Shull, J. M., & Rachford, B. L. 2002, *ApJ*, 566, 857
- Westerlund, B. E. 1990, *A&AR*, 2, 29
- Westerlund, B. E. 1997, *The Magellanic Clouds* (Cambridge, UK: Cambridge University Press), 32
- Yokogawa, J., Imanishi, K., Tsujimoto, M., et al. 2000, *ApJS*, 128, 491
- Zijlstra, A. A., Loup, C., Waters, L. B. F. M., et al., *MNRAS*, 279, 32